Article

EMBO *reports*

FTLD-TDP assemblies seed neoaggregates with subtype-specific features via a prion-like cascade

Pierre De Rossi[1,†] , Amanda J Lewis[2,†] , Johanna Furrer[1] , Laura De Vos[1] , Tomas Demeter[1] , Aurélie Zbinden[1] , Weijia Zhong[1] , Vera I Wiersma[1] , Carlo Scialo[1] , Julien Weber[1], Zhongning Guo[1], Stefano Scaramuzza[3,4], Marta Di Fabrizio[2] , Carolin Böing[3] , Daniel Castaño-Díez[4], Ashraf Al-Amoudi[3] , Manuela Pérez-Berlanga[1] , Tammaryn Lashley[5,6] , Henning Stahlberg[2] & Magdalini Polymenidou[1,*]

Abstract

Morphologically distinct TDP-43 aggregates occur in clinically different FTLD-TDP subtypes, yet the mechanism of their emergence and contribution to clinical heterogeneity are poorly understood. Several lines of evidence suggest that pathological TDP-43 follows a prion-like cascade, but the molecular determinants of this process remain unknown. We use advanced microscopy techniques to compare the seeding properties of pathological FTLD-TDP-A and FTLD-TDP-C aggregates. Upon inoculation of patient-derived aggregates in cells, FTLD-TDP-A seeds amplify in a template-dependent fashion, triggering neoaggregation more efficiently than those extracted from FTLD-TDP-C patients, correlating with the respective disease progression rates. Neoaggregates are sequentially phosphorylated with N-to-C directionality and with subtype-specific timelines. The resulting FTLD-TDP-A neoaggregates are large and contain densely packed fibrils, reminiscent of the pure compacted fibrils present within cytoplasmic inclusions in postmortem brains. In contrast, FTLD-TDP-C dystrophic neurites show less dense fibrils mixed with cellular components, and their respective neoaggregates are small, amorphous protein accumulations. These cellular seeding models replicate aspects of the patient pathological diversity and will be a useful tool in the quest for subtype-specific therapeutics.

Introduction

Frontotemporal dementia (FTD) is the most common type of dementia below the age of 65 (Harvey, 2003). It is characterized by frontotemporal lobar degeneration (FTLD) and accumulation of different pathological protein aggregates, which define its molecular classification (Lashley *et al*, 2015). FTLD-TDP subtypes represent 45% of all FTLD cases and are characterized by the accumulation and aggregation of transactive response (TAR) DNA-binding protein of 43 kDa (TDP-43) (Ling *et al*, 2013). FTLD-TDP type A (FTLD-TDP-A) pathology presents with neuronal cytoplasmic inclusions (NCI) and intranuclear inclusions, whereas FTLD-TDP type C (FTLD-TDP-C) display long and thick dystrophic neurites (Lee *et al*, 2017).

TDP-43 is an RNA-binding protein primarily localized in the nucleus, with functions in several steps of RNA metabolism (Polymenidou *et al*, 2011; Tollervey *et al*, 2011; Xiao *et al*, 2011). TDP-43 translocates to the cytoplasm where it is involved in RNA trafficking and stabilization (Ayala *et al*, 2008; Alami *et al*, 2014). Furthermore, TDP-43 forms liquid-liquid phase separated droplet-like structures in the nucleus (Murray *et al*, 2017; Guo *et al*, 2018; Maharana *et al*, 2018; Gasset-Rosa *et al*, 2019; Mann *et al*, 2019; Bhopatkar *et al*, 2020), as well as physiological oligomers through interaction of its N-terminal domains, which regulate RNA splicing (Afroz *et al*, 2017; Wang *et al*, 2018). In disease, TDP-43 forms amyloid fibrils via association of its low complexity domains at the C-terminal site (Babinchak *et al*, 2019; Cao *et al*, 2019; Shenoy *et al*, 2020; Li *et al*, 2021). Upon oxidative stress or destabilization of physiological oligomerization, nuclear droplets unmix and TDP-43 translocates to the cytoplasm where it incorporates into cytoplasmic droplets leading to cellular toxicity (Afroz *et al*, 2017; Gasset-Rosa *et al*, 2019).

---

1 Department of Quantitative Biomedicine, University of Zurich, Zurich, Switzerland
2 Laboratory of Biological Electron Microscopy, Institute of Physics, SB, EPFL, Department of Fundamental Microbiology, Faculty of Biology and Medicine, UNIL, Lausanne, Switzerland
3 C-CINA, Biozentrum, University of Basel, Basel, Switzerland
4 BioEM Lab, Biozentrum, University of Basel, Basel, Switzerland
5 Queen Square Brain Bank for Neurological diseases, Department of Movement Disorders, UCL Institute of Neurology, London, UK
6 Department of Neurodegenerative Disease, UCL Institute of Neurology, London, UK
*Corresponding author. Tel: +41 79 137 6856; E-mail: magdalini.polymenidou@uzh.ch
†These authors contributed equally to this work

One crucial question in the field is whether pathological TDP-43 follows a prion-like cascade of amplification and template-directed conversion during disease propagation (Polymenidou & Cleveland, 2011) and if so, which are the molecular determinants of this process. Several studies suggested a templating mechanism for TDP-43 *in vitro* and in cells (Nonaka *et al*, 2013; Shimonaka *et al*, 2016), its cell-to-cell propagation (Feiler *et al*, 2015), and the *in vivo* propagation of seeds through mouse brain over time (Porta *et al*, 2018, 2021). Importantly, a diagnostic tool for FTLD was recently developed based on the prion-like properties of TDP-43 *in vitro* (Scialò *et al*, 2020). We previously showed that pathological TDP-43 aggregates in patients display distinct biochemical and neurotoxic properties correlating with different disease subtypes, reminiscent of prion strains (Laferrière *et al*, 2019), a notion supported by a recent *in vivo* study (Porta *et al*, 2021). Despite all this evidence, it is still unclear whether the mechanism underlying the seeding capacity of TDP-43 depends on the structure, specific fragmentation, or posttranslational modifications of the protein.

Among the numerous potential posttranslational modifications of TDP-43 (Zbinden *et al*, 2020), phosphorylation of its C-terminal domain is the best studied, since it has long been associated with FTLD pathology (Hasegawa *et al*, 2008; Inukai *et al*, 2008; Neumann *et al*, 2009; Kametani *et al*, 2016). Phosphorylated TDP-43, or C-terminal fragments thereof, are seeding competent (Nonaka *et al*, 2016; Porta *et al*, 2018, 2021), yet the role of phosphorylation in aggregation and toxicity remains controversial. Some studies support the hypothesis that TDP-43 phosphorylation induces protein aggregation and cellular toxicity (Hasegawa *et al*, 2008; Kim *et al*, 2015; Nonaka *et al*, 2016), while others describe increased solubility and decreased toxicity for phosphorylated TDP-43, proposing that phosphorylation may be a protective cellular response (Brady *et al*, 2011; Li *et al*, 2011; preprint: Silva *et al*, 2021).

The goal of our study was to investigate the seeding potential of TDP-43 and provide direct evidence for a templating-dependent mechanism of TDP-43 propagation and the existence of distinct strains. We compared the seeding profile for individual patients with FTLD-TDP type A or C pathologies, which we previously found to have distinct biochemical and neurotoxic properties (Laferrière *et al*, 2019). Our results showed that pathological aggregates from both subtypes induced cellular neoaggregation. However, FTLD-TDP-A seeding was more potent and robust among different patients and followed a template-directed pathway. We investigated the role of phosphorylation at serines (S) 403/404 and 409/410 during seeding and showed a sequential N-to-C phosphorylation process, with unique timelines for each FTLD-TDP subtype. Importantly, we showed subtype-specific differences: while FTLD-TDP-A neoaggregates composed of large, homogeneous and densely packed fibrils, FTLD-TDP-C neoaggregates consisted of multiple small foci of amorphous protein aggregates. These were paralleled by our observations in postmortem human brain samples, where the morphological arrangement of fibrils within the aggregates differed significantly between FTLD-TDP-A and FTLD-TDP-C. Indeed, both the original FTLD-TDP-A brain aggregates and cellular neoaggregates showed a compact arrangement of homogeneous fibrils, while the FTLD-TDP-C counterparts were heterogeneous and loosely associated fibrils in patients, or completely amorphous in seeded cells. These observations were consistent with a slower rate of fibril formation in type C, compared to type A, mimicking the slower disease progression clinically observed in patients. Altogether, we observed properties of the original seeding material transpiring in the neoaggregation process, reinforcing a template-dependent mechanism of propagation involved in TDP-43 pathogenesis.

Results

FTLD patient-derived TDP-43 aggregates seed neoaggregates in cells with subtype-specific potency

To test the seeding properties of pathological TDP-43, we used our previously described experimental design (Laferrière *et al*, 2019). HEK293T cells stably expressing TDP-43-HA were transfected with pathological TDP-43 aggregates isolated from postmortem brain samples using SarkoSpin (Pérez-Berlanga *et al*, 2019). Cells were mitotically arrested to avoid losing aggregate-bearing cells over time, and were then fixed 3–6 days post-transfection. Seeding effects were analyzed using confocal imaging and Imaris reconstruction (Figs 1 and EV1A and B; Appendix Figs S1–S3). To determine if the exogenous TDP-43 aggregates introduced in cells could convert endogenous TDP-43-HA into pathological neoaggregates (NeoAgg), we quantified the colocalization of HA and TDP-43$^{pS403/404}$ (Fig 1A and B, Appendix Fig S3). We found that the number of neoaggregates progressively increased over time in cells inoculated with either FTLD-TDP-A or FTLD-TDP-C seeds, significantly more than non-neurodegenerative control seeded cells (Figs 1C and D and EV1B). In agreement with previous reports (Laferrière *et al*, 2019; Porta *et al*, 2021), seeds extracted from FTLD-TDP-A patient brains were more potent in triggering neoaggregation in cells, with FTLD-TDP-C seeds showing a large patient-to-patient variability (Fig 1C and D). Interestingly, neoaggregates had different morphologies between type A and C transfected cells, revealing single and large cytoplasmic aggregates for type A, versus multiple smaller aggregates for type C (Figs 1B and EV1C).

TDP-43 pathology in patients is often accompanied by loss of nuclear TDP-43, termed nuclear clearance (Arai *et al*, 2006; Neumann *et al*, 2006), and loss of TDP-43 function (Ling *et al*, 2015; Klim *et al*, 2019; Melamed *et al*, 2019). To determine if neoaggregate formation in our model also triggered nuclear clearance, we quantified nuclear TDP-43 over time, defined by the colocalization between TDP-43-HA and DAPI. We found a progressive loss of nuclear TDP-43 in patient-derived SarkoSpin-inoculated cells (Figs 1A and EV1D–F). Nuclear clearance of TDP-43 was accompanied by changes in the nuclear morphology. Nuclei of both FTLD-TDP-A and FTLD-TDP-C seeded cells became more round compared to control cells, as evidenced by the significant increase of their sphericity and the reduction of their oblate axis, while the prolate axis remained unchanged (Fig EV1G–J).

To explore whether cells with neoaggregates were the same as the ones with TDP-43 nuclear clearance, we computed the distance between neoaggregates and either DAPI alone or nuclear TDP-43 at days 3 and 6 post seeding (Fig EV1K–M). Neoaggregates analyzed at both time points showed close proximity to DAPI (Fig EV1K–M, dashed lines), suggesting preferential cytoplasmic localization. However, neoaggregate proximity to nuclear TDP-43 decreased over time (Fig EV1K–M, full lines) indicating that cells with pathological cytoplasmic neoaggregates were losing nuclear TDP-43. Both
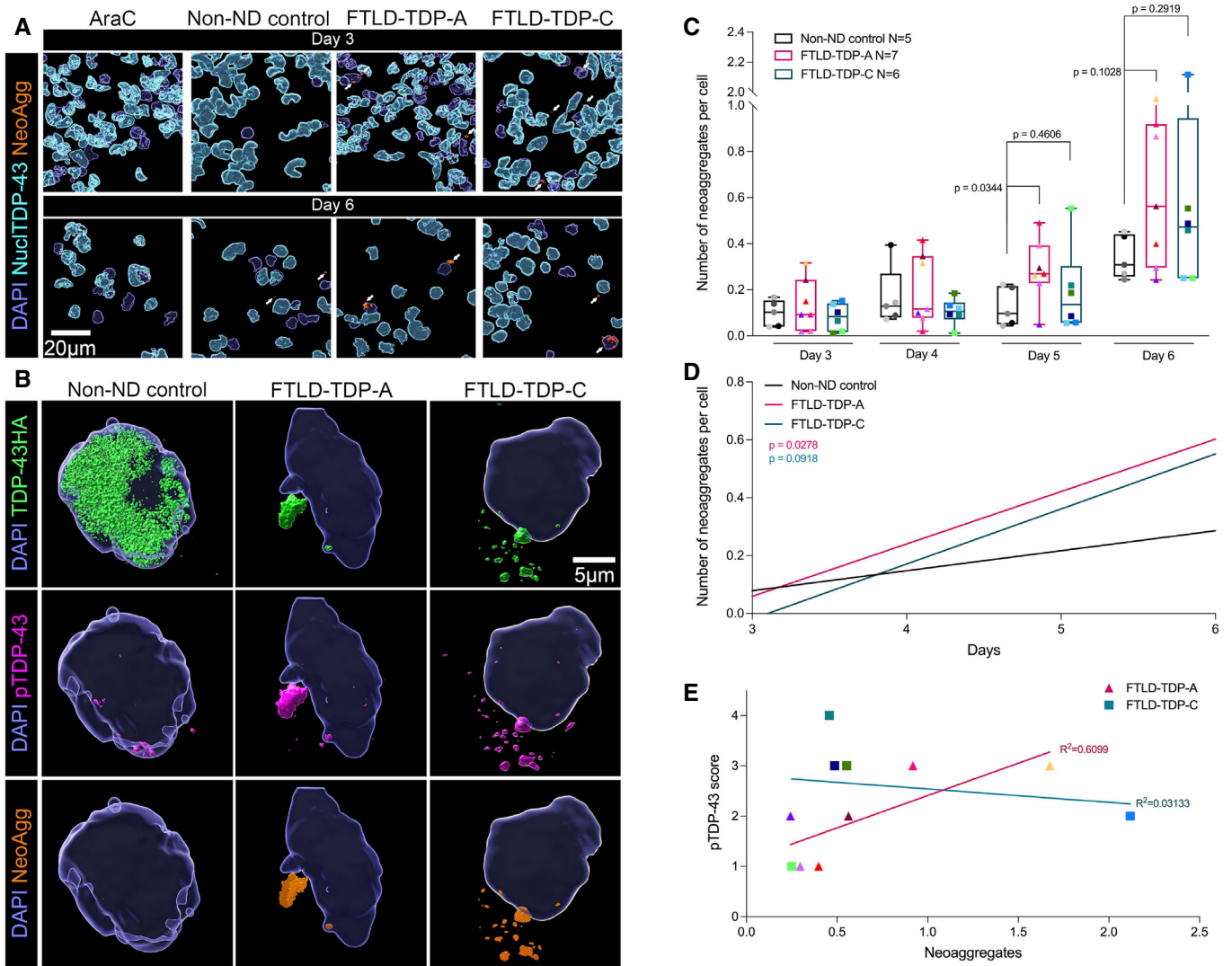
Figure 1. FTLD patient-derived TDP-43 aggregates seed neoaggregates in cells with subtype-specific potency.

A   Seeding efficiency was compared between control non-neurodegenerative (non-ND) and FTLD-TDP patient samples. Cells were transfected using Lipofectamine after mitotic arrest with AraC and were fixed 3–6 days post-transfection with SarkoSpin fractions (Laferrière *et al*, 2019). Surface masks generated with Imaris show DAPI (blue), nuclear TDP-43 (NuclTDP-43, cyan) and neoaggregates (NeoAgg, orange). All images are presented at the same scale, 20 μm as indicated in AraC panel Day 6.

B   Higher magnification imaging of cells seeded for 6 days revealed presence of large cytoplasmic TDP-43-HA aggregates in cells seeded with FTLD-TDP-A and multiple cytoplasmic TDP-43-HA aggregates in cells seeded with FTLD-TDP-C. Surface representation generated with Imaris showing DAPI, TDP-43-HA (green), phosphorylated TDP-43 (pTDP-43, magenta) and neoaggregates (NeoAgg, orange). All images are presented at the same scale, 5 μm as indicated in FTLD-TDP-C top panel.

C   Quantification of the number of neoaggregates over time in (*n* = 3) independent experiments, with multiple biological replicates: non-ND control (*n* = 5), FTLD-TDP-A (*n* = 7) and FTLD-TDP-C (*n* = 6). Whiskers in the box plot represent median and minimum/maximum values. 2-way ANOVA repeated measure, with post-hoc Fisher's LSD, $F_{(3,15)} = 1.3$, $P = 0.3110$, NS difference for Day 3 and 4. Day 5: Non-ND control vs FTLD-TDP-A $P = 0.0344$, non-ND control vs FTLD-TDP-C $P = 0.4606$. Day 6: non-ND control vs FTLD-TDP-A $P = 0.1028$, non-ND control vs FTLD-TDP-C $P = 0.2919$.

D   Linear regression model of neoaggregate formation over time. Best-fit values: non-ND control ($y = 0.06902x - 0.1281$, $R^2 = 0.3655$, $P = 0.0048$), FTLD-TDP-A ($y = 0.1810x - 0.4836$, $R^2 = 0.3532$, $P = 0.0009$), FTLD-TDP-C ($y = 0.1902x - 0.5896$, $R^2 = 0.2581$, $P = 0.0112$). Null-hypothesis slope=0.06902: non-ND control vs FTLD-TDP-A $P = 0.0278$, non-ND control vs FTLD-TDP-C $P = 0.0918$.

E   Comparison of pTDP-43 score to neoaggregate formation per patient showed positive correlation for FTLD-TDP-A and no correlation for FTLD-TDP-C. Trendline is shown per subtype. Best-fit value of linear regression model: FTLD-TDP-A ($y = 1.286x + 1.123$, $R^2 = 0.6099$, $P = 0.0667$), FTLD-TDP-C ($y = -0.2655x + 2.805$, $R^2 = 0.03133$, $P = 0.7758$).

neoaggregate formation and nuclear clearance of TDP-43 were observed in control conditions, suggesting that cellular stress can trigger these events, as previously suggested (Gasset-Rosa *et al*, 2019). However, the occurrence of neoaggregates (Fig 1C–E) and nuclear clearance (Fig EV1D–F) was significantly lower in the controls compared to cells inoculated with patient-derived aggregates. Importantly, we found that the seeding potency of FTLD type A, but not type C, extracts correlated with the degree of TDP-$43^{pS409/410}$ load in the same patients (Fig 1E), as determined by western blot (Laferrière *et al*, 2019). In contrast, we found no

correlation with disease duration, sex of the patient or disease-associated mutations (Fig EV1N–P). Collectively, our data indicate that FTLD-TDP-A and FTLD-TDP-C patient-derived TDP-43 aggregates trigger neoaggregation and nuclear clearance with distinct potencies, potentially via different mechanisms.

TDP-43 seeding depends on specific aggregate conformation(s)

The progressive increase in neoaggregate formation upon inoculation with patient-derived aggregates suggested a prion-like mechanism, which was proposed to mediate the pathological TDP-43 amplification during disease progression (Polymenidou & Cleveland, 2011; Brettschneider et al, 2013). To address this question, we first denatured the seeds with temperature and pressure, in order to disrupt their three-dimensional conformation (Fig 2A), which is necessary for template-dependent conversion (Aguzzi & Polymenidou, 2004). We focused on FTLD-TDP-A, as this subtype provided the most consistent seeding effect, both in this study (Fig 1C) and in a recently published independent report (Porta et al, 2021). While untreated seeds induced neoaggregation, confirming our previous observations, both thermal denaturation and a combination of heat and pressure (autoclaving) abolished the seeding effect of FTLD-TDP-A (Fig 2B).

To test if the protein alone could induce aggregation in cells, we generated recombinant TDP-43 aggregates in vitro. We produced and purified human TDP-43 fused with the solubilization tag Maltose-Binding Protein (MBP), following an established protocol (Wang et al, 2018). Upon enzymatic cleavage of MBP, the released TDP-43 rapidly aggregated in vitro. Thioflavin T (ThT) staining and electron microscopy revealed the amorphous structure of the in vitro-generated aggregates, which were rich in beta sheets (labeled by ThT) (Fig 2C). Increasing protein amounts of these amorphous in vitro-generated aggregates were transfected in cells following the same seeding protocol used for patient material (Fig EV1A). While we detected no neoaggregation, we observed a dose-dependent increase in TDP-43$^{pS403/404}$ positive foci in cells transfected with recombinant aggregates (Fig 2D and E), compatible with the notion that internalized exogenous aggregates become phosphorylated inside cells. The decrease in the TDP-43$^{pS403/404}$ signal, observed at the highest concentrations used (2.5 and 5 µg), may be due to limited internalization efficiency for larger protein amounts. Taken together, these data indicated that seeding relied on specific aggregate conformation(s) and that when these were experimentally abolished (denaturation of patient material), or failed to generate (amorphous recombinant aggregates), cellular neoaggregation was absent.

Phosphorylation of TDP-43 occurs sequentially from N- to C-terminal sites with a subtype-specific timeline

An alternative explanation for the seeding incompetence of the in vitro-generated TDP-43 aggregates is that seeding might depend on phosphorylation (Nonaka et al, 2016), which is absent from the bacterially produced protein. Phosphorylation at the extreme C-terminal serines 403/404 and 409/410 (Hasegawa et al, 2008; Inukai et al, 2008; Neumann et al, 2009) has long been known to occur in aggregates of amyotrophic lateral sclerosis (ALS) and FTLD patients (Neumann et al, 2006), and TDP-43$^{pS409/410}$ is routinely used for

postmortem neuropathological diagnosis. To understand the role of phosphorylation at these two positions, we investigated their occurrence and distribution over time within FTLD-TDP-A and FTLD-TDP-C neoaggregates.

We quantified the number of neoaggregates bearing only pS403/404, only pS409/410 or both at the same time (Fig 3A and B). We observed a significant increase in p403/404 levels in all conditions at day 4 post transfection, and a slow sequential decrease thereafter, suggesting that this specific site of phosphorylation could be linked to cellular stress response (Fig 3B). In non-neurodegenerative control-inoculated cells, no other phosphorylated TDP-43 population showed significant increase during the experimental timeline. In contrast, in cells inoculated with pathological TDP-43 derived from patient brains, an increase in neoaggregates containing either pS409/410 alone or both marks were observed over time. The initial pS403/404 spike, followed by the gradual increase in pS409/410 and bi-phosphoryated neoaggregates suggested a maturation process during which pS403/404 occurred before pS409/410. In FTLD-TDP-C-inoculated cells, both single pS403/404 and bi-phosphorylated neoaggregates (FTLD-TDP-C, pS403/404-409/410, 3 vs 4, $P = 0.0522$) were already increased at day 4. In contrast, in type A, the increase in bi-phosphorylated neoaggregates was observed at later timepoints, day 5 and 6 (FTLD-TDP-A, pS403/404-409/410, 3 vs 5, $P = 0.0577$, 3 vs 6, $P = 0.0609$), suggesting a distinct phosphorylation timeline in the two subtypes. Notably, our data indicate that in FTLD-TDP-C neoaggregates, the pS409/410 event depends on phosphorylation of pS403/404, but not vice versa, as we observed a steady increase in the number of bi-phosphorylated neoaggregates from day 3 to day 6, while the number of p409/410 decreased at day 6 (Fig 3B). In contrast, in FTLD-TDP-A-seeded cells, the two sites may be phosphorylated independently, as we observe an increase of both p409/410 and bi-phosphorylated neoaggregates from day 3 to day 6 (Fig 3B). In line with that, at day 6, the percentage of pS409/410 neoaggregates that were also phosphorylated on pS403/404 was 75% for FTLD-TDP-C, but only 40% for FTLD-TDP-A (Fig 3C). Moreover, size analysis revealed that pS409/410-positive neoaggregates (including pS409/410 alone or double phosphorylated) were larger than their pS403/404-positive counterparts at both time points and for both subtypes (Fig 3D), compatible with a maturation process in which pS403/404 occurs prior to pS409/410. Nevertheless, pS403/404-positive neoaggregates were significantly larger in FTLD-TDP-A-seeded cells compared to FTLD-TDP-C, as we previously found (Fig EV1C). This difference may be due to different structures of the neoaggregates and differential accessibility of the phosphorylation sites in the two subtypes. It is conceivable that as the aggregates mature and grow in size, one phosphorylation is favored over the other, and in turn, phosphorylation might influence aggregate structure, as recently proposed (Li et al, 2021).

To directly test the interdependence of pS403/404 and pS409/410 phosphorylation sites, we used motor neuron-like NSC-34 cells, in which overexpression of GFP-TDP-43^{WT} suffices to induce phosphorylation and aggregation (Fig 3E), as we previously showed (Afroz et al, 2017). For each 403/404 and 409/410 site, we generated phosphomimetic (serine substitution to aspartic acid or glutamic acid) or phosphoblocking (serine substitution to cysteine or alanine) variants of GFP-TDP-43. Antibodies against TDP-43$^{pS403/404}$ or TDP-43$^{pS409/410}$ showed no specific signal for
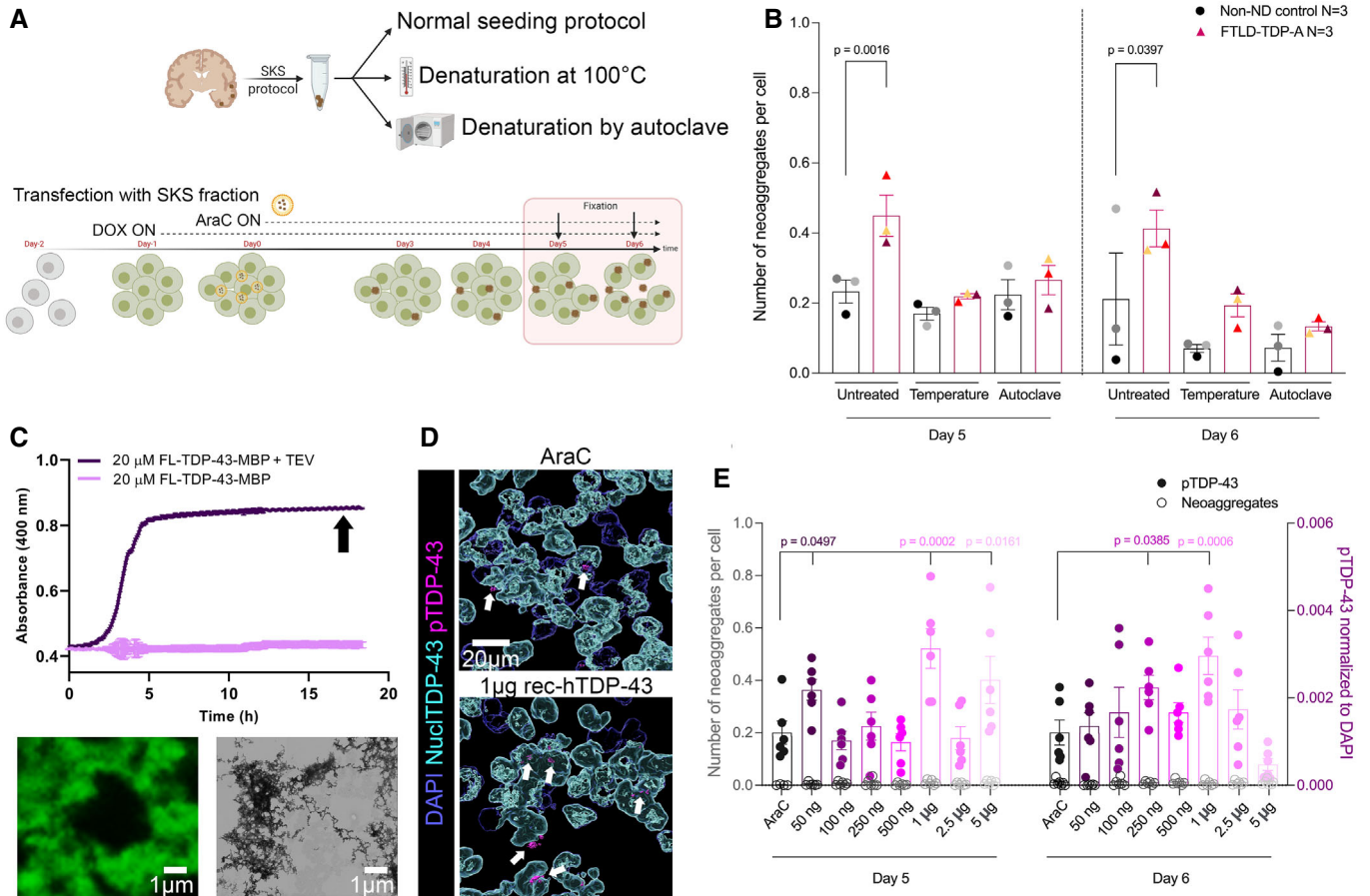
Figure 2. TDP-43 seeding depends on specific aggregate conformation(s).

A Strategy to explore the prion-like properties of TDP-43 seeds.

B Bar graph showing the seeding effect at day 5 and day 6 post-seeding in untreated, temperature denaturation or autoclaving denaturation conditions. While seeding in untreated condition showed a significant increase in neoaggregates (One-way ANOVA, with post-hoc Fisher's LSD test, Day 5: $F_{(5,12)}$ = 6.713, P = 0.0033, non-neurodegenerative (non-ND) control vs FTLD-TDP-A P = 0.0016, Day 6: $F_{(5,12)}$ = 4.271, P = 0.0183, non-ND control vs FTLD-TDP-A P = 0.0397), this effect was abolished in denaturing conditions (N = 3 biological replicates for non-ND control, FTLD-TDP-A and FTLD-TDP-C, bar graph showing mean ± SEM).

C TOP: Aggregation kinetics of full length (fl) recombinant human TDP-43 (rec-hTDP-43) measured as an increase in absorbance. The addition of TEV protease induces the cleavage of the MBP tag and subsequent aggregation of rec-hTDP-43. Rec-hTDP-43 aggregates used for seeding were collected 18 h after the addition of TEV protease. BOTTOM LEFT: rec-hTDP-43 aggregates stained by Thioflavin T (ThT). BOTTOM RIGHT: Transmission Electron Microscopy (TEM) image of the rec-hTDP-43 aggregates. All images are presented at the same scale of 1 µm.

D Rec-hTDP-43 aggregates were transfected on mitotically arrested cells and fixed after 5 or 6 days post-transfection. Surface masks generated with Imaris depict DAPI (blue), NuclTDP-43 (cyan) and pTDP-43 (magenta) for non-transfected AraC control and 1 µg rec-hTDP-43. All images are presented at the same scale, 20 µm as indicated in AraC panel.

E Quantification of neoaggregates (left y-axis) and pTDP-43 (right y-axis) at day 5 and day 6 post-transfection for increasing concentrations of rec-hTDP-43. 2-way ANOVA repeated measure, with post-hoc Fisher's LSD, $F_{(7,80)}$ = 5.886, P < 0.0001, Day 5: AraC vs 50 ng P = 0.0497, AraC vs 500 ng P = 0.0002, AraC vs 5 µg P = 0.0161. 50 ng vs 100 ng P = 0.0208, 50 ng vs 500 ng P = 0.0169, 50 ng vs 2.5 µg P = 0.0272, 100 ng vs 1 µg P < 0.0001, 100 ng vs 5 µg P = 0.006, 250 ng vs 1 µg P = 0.0005, 250 ng vs 5 µg P = 0.034, 500 ng vs 1 µg P < 0.0001, 500 ng vs 5 µg P = 0.0047, 1 µg vs 2.5 µg P < 0.0001, 2.5 µg vs 5 µg P = 0.0081, Day 6: AraC vs 250 ng P = 0.0385, AraC vs 1 µg P = 0.0006, 50 ng vs 1 µg P = 0.0016, 100 ng vs 1 µg P = 0.0101, 100 ng vs 5 µg P = 0.0173, 250 ng vs 5 µg P = 0.0006, 500 ng vs 1 µg P = 0.0099, 500 ng vs 5 µg P = 0.0176, 1 µg vs 2.5 µg P = 0.0144, 1 µg vs 5 µg P < 0.0001, 2.5 µg vs 5 µg P = 0.0121. To reduce complexity, only comparisons with AraC are marked in the graph. N = 6 biological replicates for each concentration; bar graph showing mean ± SEM.

the variants with mutations within the respective sites, possibly due to interference with their epitope. Interestingly, while phosphorylation of 409/410 did not affect phosphorylation of 403/404, blocking of 403/404 also blocked phosphorylation of 409/410. Additionally, mimicking 403/404 phosphorylation led to enhanced phosphorylation at 409/410 (Fig 3E). These observations indicate that phosphorylation within the low complexity region of TDP-43 occurs sequentially from N-terminal to C-terminal sites (Fig 3F), in line with the mode of substrate recognition of Casein Kinase I

(Vielhaber & Virshup, 2001), the main kinase phosphorylating TDP-43 in patients (Krach *et al*, 2018). However, this directionality may be lost upon fibril formation. Indeed, a recent cryoEM structure of amyloid fibrils formed by the TDP-43 low complexity domain suggests that hyperphosphorylation of TDP-43 would impose steric hindrance during fibril formation leading to fibril structure polymorphism (Li *et al*, 2021). Therefore, the differential phosphorylation we observed for FTLD-TDP-A and FTLD-TDP-C could underlie disease subtype heterogeneity.
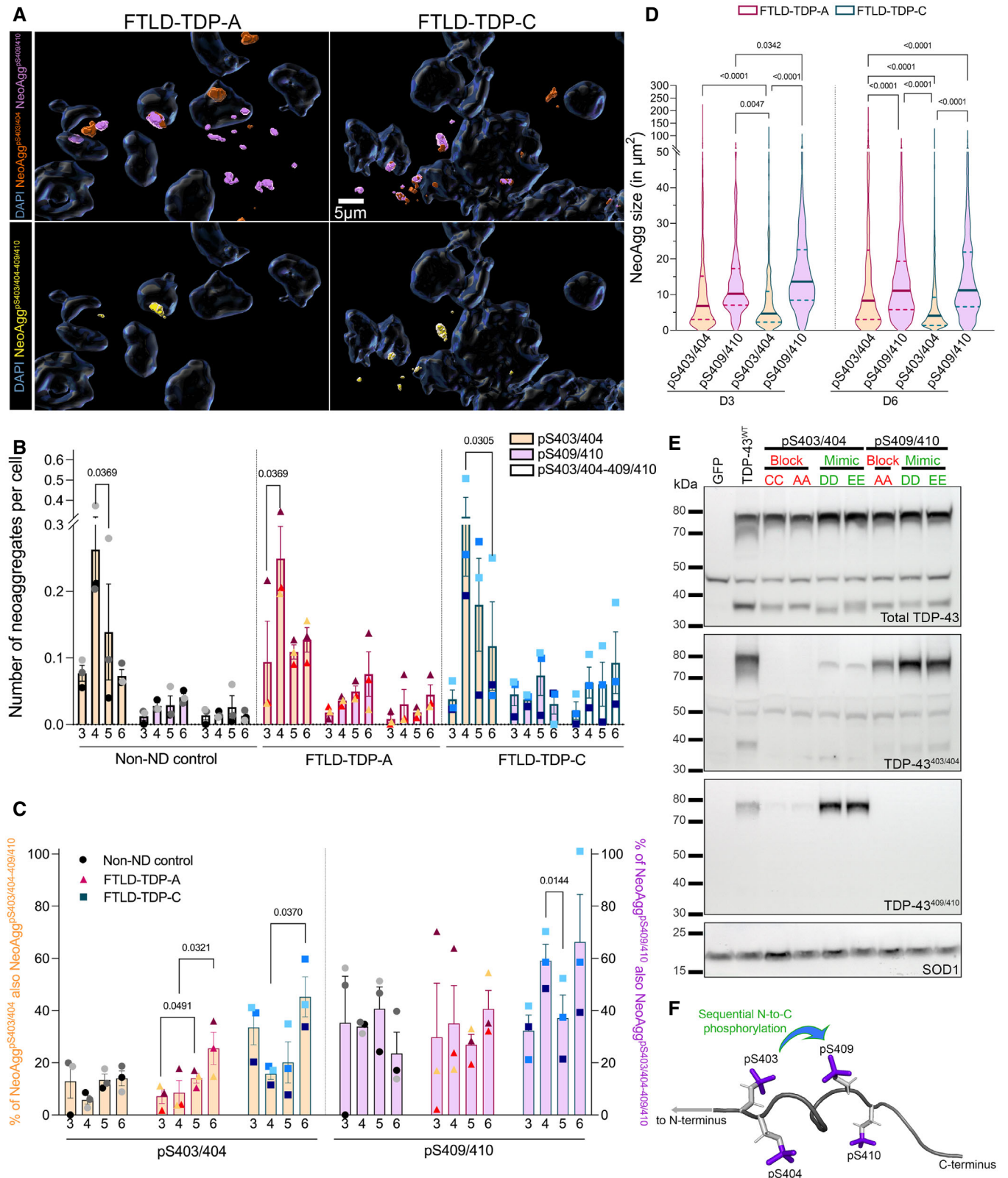
Figure 3.

Figure 3. Phosphorylation of TDP-43 occurred sequentially from N- to C-terminal sites and showed a subtype-specific timeline.

A Analysis of neoaggregation in HEK cells (similar method as Fig 1 and Appendix Fig S3) using Imaris. Images represent field of view for FTLD-TDP-A seeded cells (left) and FTLD-TDP-C seeded cells (right) and labeled with DAPI (transparent blue), neoaggregates phosphorylated at S403/404 (NeoAgg^{pS404}, orange) and neoaggregates phosphorylated at S409/410 (NeoAgg^{pS409}, light purple). Bottom panel shows neoaggregates bearing double phosphorylation S403/404 and S409/410 (NeoAgg$^{pS404-409}$, yellow). All images are presented at the same scale, 5 μm as indicated in FTLD-TDP-C panel.

B Bar graphs representing the number of NeoAgg^{pS403} only (bars filled in light orange), NeoAgg^{pS409} only (bars filled in light purple) and double phosphorylated NeoAgg$^{pS403-409}$ (unfilled bars) for each condition. Individual patients are labeled in different colored dots (n = 3 biological replicates for each condition, graph bar showing mean ± SEM. Two-way ANOVA repeated measures, with post-hoc Fisher's LSD test, F(24.54) = 3.799, P < 0.0001, Day 4: non-neurodegenerative (non-ND) control pS403/404 vs pS409/410, P < 0.0001, non-ND control pS403/404 vs bi-phosphorylated, P < 0.0001, FTLD-TDP-A pS403/404 vs pS409/410, P < 0.0001, FTLD-TDP-A pS403/404 vs bi-phosphorylated, P < 0.0001 FTLD-TDP-C pS403/404 vs pS409/410, P < 0.0001, FTLD-TDP-C pS403/404 vs bi-phosphorylated, P < 0.0001. Day 5: non-ND control pS403/404 vs bi-phosphorylated, P = 0.0219, FTLD-TDP-A pS403/404 vs double, P = 0.0650, FTLD-TDP-C pS403/404 vs double, P = 0.0157. Day 6: Control bi-phosphorylated vs FTLD-TDP-A bi-phosphorylated, P = 0.5096, control bi-phosphorylated vs FTLD-TDP-C, P = 0.1010. Non-ND control pS403/404: day 3 vs 4, P = 0.0559, day 3 vs 6, P = 0.0369. FTLD-TDP-A pS404/404, day 3 vs 4, P = 0.0075, day 4 vs 5, P = 0.0714. FTLD-TDP-C pS403-404, day3 vs 4, P = 0.0759, day 4 vs 6, 9 = 0.0305. FTLD-TDP-A bi-phosphorylated: day 3 vs 5, P = 0.0577, day 3 vs 6, P = 0.0609. FTLD-TDP-C bi-phosphorylatede: day 3 vs 4, P = 0.0522.

C Bar graph representing the percentage of NeoAgg$^{pS403/404}$ bearing double phosphorylation (left side, bars filled in light orange) and percentage of NeoAgg^{pS409} bearing double phosphorylation (right side, bars filled in light purple). Each individual patient is labeled in different colored dots. N = 3 biological replicates per condition, graph bar showing mean ± SEM. Two-way ANOVA repeated measures, with post-hoc Fisher's LSD test, pS403/404 also double positive: F(3,6) = 6.567, P = 0.0253: FTLD-TDP-A: Day 3 vs 5, P = 0.0491, day 4 vs 6, P = 0.0321, FTLD-TDP-C: ay 4 vs 6, P = 0.037. pS409/419 also double positive: F(3,6) = 1.246, P = 0.3731, FTLD-TDP-C: Day 4 vs 5, P = 0.0144.

D Violin graph representing the area of NeoAgg404 (filled in light orange) and NeoAgg409 (filled in light purple) at day 3 and day 6 post seeding with FTLD-TDP-A and C seeds. Full bar represent median values, dashed lines represent quartiles. Two-way ANOVA with *post hoc* Fisher's LSD test, day 3: FTLD-TDP-A vs FTLD-TDP-C NeoAgg^{pS404} P < 0.0001, FTLD-TDP-A vs FTLD-TDP-C NeoAgg^{pS409} P = 0.0342, FTLD-TDP-A NeoAgg^{pS409} vs FTLD-TDP-C NeoAgg^{pS404} P = 0.0047, FTLD-TDP-C NeoAgg^{pS404} vs NeoAgg^{pS409} P < 0.0001; Day 6: FTLD-TDP-A vs FTLD-TDP-C NeoAgg^{pS404} P < 0.0001, FTLD-TDP-A NeoAgg^{pS409} vs FTLD-TDP-C NeoAgg^{pS404} P < 0.0001, FTLD-TDP-A NeoAgg^{pS404} vs FTLD-TDP-C NeoAgg^{pS409} P < 0.0001, FTLD-TDP-A NeoAgg^{pS404} vs NeoAgg^{pS409} P < 0.0001, FTLD-TDP-C NeoAgg^{pS404} vs NeoAgg^{pS409} P < 0.0001.

E Overexpression of GFP-TDP-43 variants with different mutations that either block (CC and AA mutation, red labels) or mimic phosphorylation (DD and EE, green label) at S403/404 or S409/410 in motor neuron-like NSC-34 cells. Western blot showed a specific signal for total TDP-43 (top panel), TDP-43$^{pS403/404}$ (middle panel) and TDP-43$^{p409/410}$ (lower panel) and load control SOD1 (bottom panel).

F Schematic of the extreme C-terminal serine phosphorylation found in pathological TDP-43.

Distinct features of cellular neoaggregates resemble subtype-specific characteristics in FTLD brains

To explore the differences between type A and type C neoaggregates, we first used superresolution microscopy at day 6 post inoculation with SarkoSpin extracts. We combined staining for TDP-43-HA and markers of the nuclear envelope to determine its integrity in aggregate-bearing cells. This analysis revealed that in cells with both types of neoaggregates, the nuclear envelope was compromised and that LaminB1 and Nucleopore complexes were sequestered by the neoaggregates (Fig 4A and B), in agreement with previously published data (Chou *et al*, 2018). Moreover, we observed that tubulin was also sequestered by the neoaggregates (Fig EV2A), suggesting a potential disruption of the cytoskeleton. However, a nucleolar marker was not found within the neoaggregates (Figs 4C and EV2B), confirming the specificity of our observations. Interestingly, the degree of coaggregation of the different markers with TDP-43 neoaggregates differed between the two subtypes. Quantification revealed that FTLD-TDP-C neoaggregates contained nuclear proteins more frequently than FTLD-TDP-A, while the opposite was true for tubulin (P = 0.0615) (Fig EV2B). These results suggested potentially distinct toxic mechanisms of TDP-43 type A versus type C neoaggregates via destabilization of the cytoskeleton organization, or disorganization of the nuclear envelope, respectively.

We then compared the density of particles—defined as the number of particles per area unit—for each type of neoaggregate using

Figure 4. Superresolution analysis shows distinct features of type A and C cellular neoaggregates.

A–C dSTORM images of cells seeded for 6 days with non-neurodegenerative control (non-ND control), FTLD-TDP-A and FTLD-TDP-C seeds extracted from post-mortem brain tissue. Staining shows localization of TDP-43 (HA tag, cyan) along with LaminB1 (yellow, A), nucleopore complexes (nucleopores, yellow, B) and nucleolus (yellow, C). Cells seeded with FTLD-TDP seeds show coaggregation of nuclear membrane proteins upon neoaggregate formation. All images are presented at the same scale, 2 μm as indicated in the non-neurodegenerative control top panels.

D dSTORM images of cells containing aggregates after 6 days of seeding with SarkoSpin fractions of postmortem brain from patients with FTLD-TDP-A or FTLD-TDP-C. Red arrows point to cytoplasmic aggregates. Cells were labeled with TDP-43 (HA-tag, cyan) and phosphorylated TDP-43 pS403/404 (pTDP-43, magenta). All images are presented at the same scale, 2 μm as indicated in the FTLD-TDP-A top panel.

E Violin plots showing the size of analyzed neoaggregates using TDP-43-HA area. Non-parametric unpaired *t*-test FTLD-TDP-A vs FTLD-TDP-C, P < 0.0001. (Continuous line represent median, dashed lines represent quartiles, n = 3 independent experiments, six biological replicates for each condition).

F Bar graph showing the number of neoaggregates per cell. Non-parametric unpaired *t* test FTLD-TDP-A vs FTLD-TDP-C, P = 0.0003. Error bars represent mean ± SEM, n = 3 independent experiments, six biological replicates for each condition.

G Heatmap representation of the density of TDP-43-HA and pTDP-43 particles for four representative neoaggregates of FTLD-TDP-A and FTLD-TDP-C seeded cells. All images are presented at the same scale, 1 μm as indicated in the FTLD-TDP-C top right panel.

H Violin plots showing the density of particles TDP-43 per μm^2. Non-parametric unpaired *t* test FTLD-TDP-A vs FTLD-TDP-C, P = 0.0083. (Continuous line represent median, dashed lines represent quartiles, n = 3 independent experiments, six biological replicates for each condition).
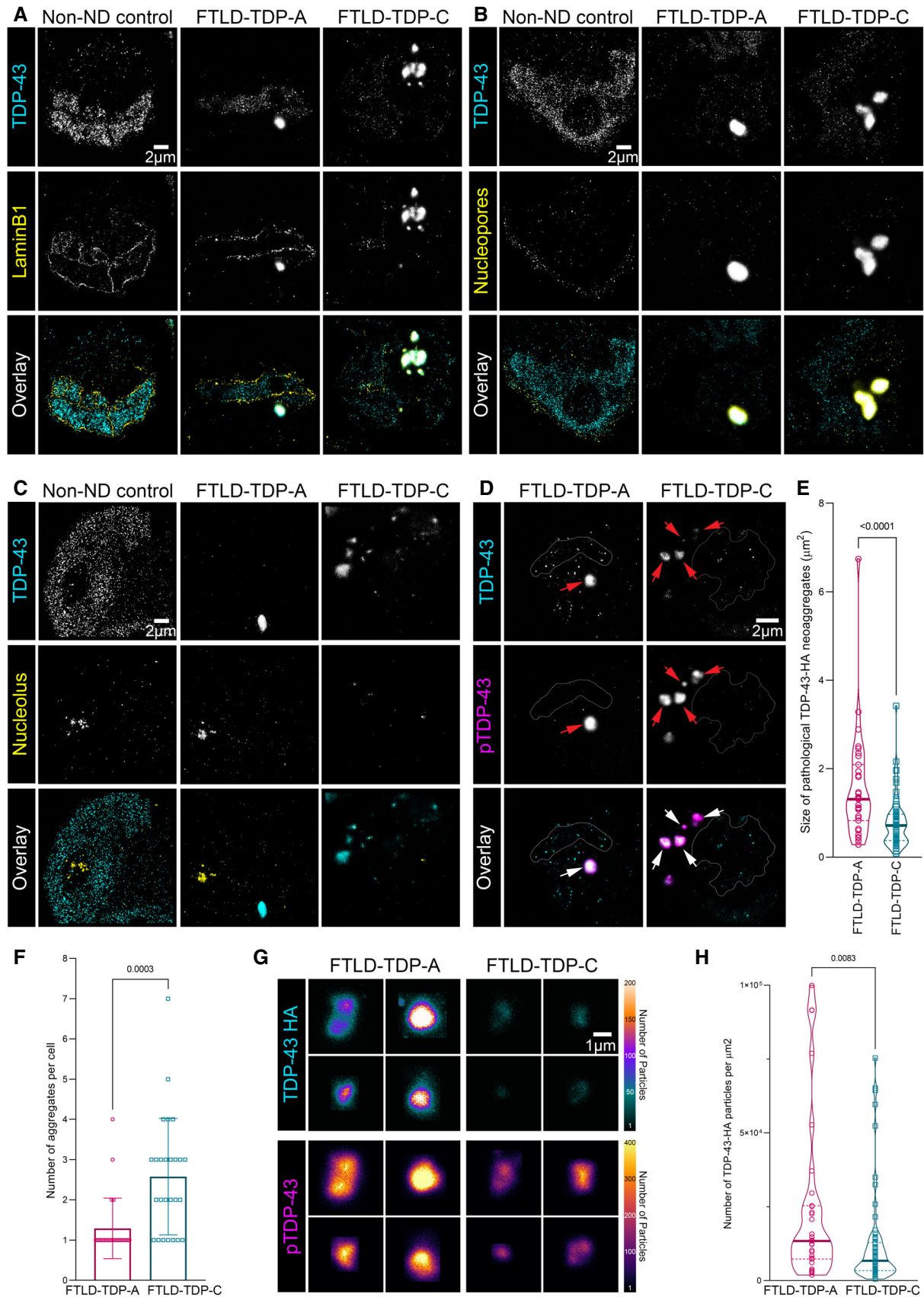
Figure 4.

both TDP-43-HA and TDP-43$^{pS403/404}$ (Fig 4D). Confirming our previous observation by confocal imaging (Fig EV1C), dSTORM analysis revealed that pathological neoaggregates of type A were larger than type C (Figs 4E and EV2C), and the latter tended to develop multiple neoaggregates per cell, in contrast to single type A neoaggregates (Fig 4F). Importantly, type A TDP-43-HA neoaggregates showed higher density of particles compared to type C (Fig 4G and H), albeit this observation did not reach statistical significance when we probed phosphorylated TDP-43$^{pS403/404}$ neoaggregates (Fig EV2D). Together, these results suggested that seeding with patient-derived TDP-43 aggregates resulted in neoaggregates with different properties, potentially resembling the original aggregates in the seeds.

In order to assess the ultrastructure of the cellular neoaggregates, we utilized correlative light and electron microscopy (CLEM) (Fig EV3A–C). HEK cells were prepared for EM and an anti-HA antibody was used to detect cellular neoaggregates. By light microscopy, pathologically seeded cells showed intracellular, HA-immunopositive aggregates 2–3 μm in size for FTLD-TDP-A and ~1 μm in size for FTLD-TDP-C (Fig 5, LM), consistent with previous fluorescent microscopy observations. No HA-immunopositive neoaggregates were observed in non-neurodegenerative control-seeded cells.

In FTLD-TDP-A-seeded cells, we correlated four HA-immunopositive aggregates by EM that corresponded to accumulated fibrils (Fig 5A, Appendix Fig S4A). FTLD-TDP-A neoaggregate fibrils were arranged in random orientation, both horizontally and perpendicular to the electron beam. Occasionally, the HA-immunopositive fibrils were observed among regions of other filamentous material, which were visibly thinner and displayed a more ordered and linear arrangement (Appendix Fig S4A). Regions showing a similar ordered arrangement of filaments were observed in cells seeded with non-neurodegenerative controls (Appendix Fig S4B), albeit in regions without HA immunopositivity. Given our previous observations showing that neoaggregates co-localized with tubulin (Fig EV2A and B), we reasoned that these filaments were cytoskeletal components of HEK cells.

In contrast to FTLD-TDP-A neoaggregates, HA-immunopositive regions in FTLD-TDP-C-seeded cells did not contain fibrils. While multiple HA-immunopositive neoaggregates were detected in FTLD-TDP-C-seeded cells by light microscopy and the same neoaggregate-containing cell was localized by EM, there was no characteristic ultrastructure that could distinguish the immunopositive area from the surrounding cellular material. As such, only a single FTLD-TDP-C-seeded neoaggregate could be successfully correlated with an ultrastructure via EM, which showed amorphous accumulation of proteinaceous material (Fig 5B, EM). The data suggest that TDP-43-HA was in the early stages of aggregation such that higher order structures had not yet formed.

Fibril organization and cellular microenvironment differentiate FTLD-TDP-A from FTLD-TDP-C aggregates in patients

Collectively, our observations with superresolution microscopy and CLEM supported the notion that type A and type C neoaggregates have distinct ultrastructures. Since our data indicated a template-directed mechanism of neoaggregate formation, we reasoned that these differences originated from the patient-derived seeds. TDP-43 pathology differs significantly between FTLD-TDP-A and FTLD-TDP-C in human brain; however, no ultrastructural features have previously been described that could account for the differences we observed in our cell model. Therefore, we investigated the ultrastructure of TDP-43 pathology in the postmortem human brain using advanced microscopy techniques.

We first focused on the NCIs characteristic of FTLD-TDP-A pathology (Lee et al, 2017). To characterize the ultrastructure of NCIs, we utilized the same CLEM strategy as for the cellular neoaggregates (Fig EV3). We localized and characterized five TDP-43 immunopositive NCIs in four FTLD-TDP-A brain donors (Fig 6A and EV4A–E). By light microscopy, the NCIs from FTLD-TDP-A were round and compact, measuring 3–6 μm in diameter. By EM, the ultrastructure of the same TDP-43-immunopositive regions corresponded to densely packed fibrils. Interestingly, the fibrils appeared to be encircled by a membrane, which appeared to be distinct from both the nuclear and cell membrane (Figs 6A and EV4A–E). In cases with long postmortem delay, we observed that the membrane surrounding the NCIs was often fragmented or disrupted but still detectable (Fig EV4B, D and E).

We next asked if this membrane surrounding the NCIs could be of nuclear origin given our previous observations in HEK cells that the FTLD-TDP-seeded neoaggregates colocalized with nuclear envelope proteins. Using STED light microscopy, we identified colocalization of LaminB1 within the FTLD-TDP-A NCIs (Fig 6B). These observations are consistent with previously published data suggesting TDP-43 pathology leads to the disruption of key nuclear membrane structures (Chou et al, 2018).

In contrast to FTLD-TDP-A, the most common FTLD-TDP-C pathological feature is not NCIs, but long dystrophic neurites, which may form within either axons or dendrites (Lee et al, 2017). To clarify the subcellular origin of FTLD-TDP-C dystrophic neurites, we compared the colocalization of pathological TDP-43 with a dendritic (MAP2) to an axonal (phospho-neurofilament (PNF)) marker by confocal light microscopy (Fig 6C). Interestingly, we could not identify dystrophic neurites colocalizing with MAP2 (Fig 6C, top and middle panels), suggesting that the neurites were not of dendritic origin. Instead, dystrophic neurites colocalized with PNF-positive structures (Fig 6C, lower panels), indicating an axonal origin for FTLD-TDP-C pathology.

Figure 5. Correlative light and electron microscopy shows distinct features of type A and C cellular neoaggregates.

Light microscopy images (LM) showing the HA-immunoreactive inclusions (green color, black arrowheads) identified in ultrathin sections from resin-embedded cell monolayers. The LM images were overlaid with low magnification EM images (EM/LM overlay) to localize the same region within the cells for EM imaging at higher magnification (dotted black square, EM).

A HA-immunopositive regions within cells seeded with FTLD-TDPA patient material showed accumulated filaments (examples indicated with white arrowheads).

B HA-immunopositive regions within cells seeded with FTLD-TDP-C patient material showed aggregated amorphous material. Scale bars LM and EM/LM overlay, 10 μm; EM, 500 nm.
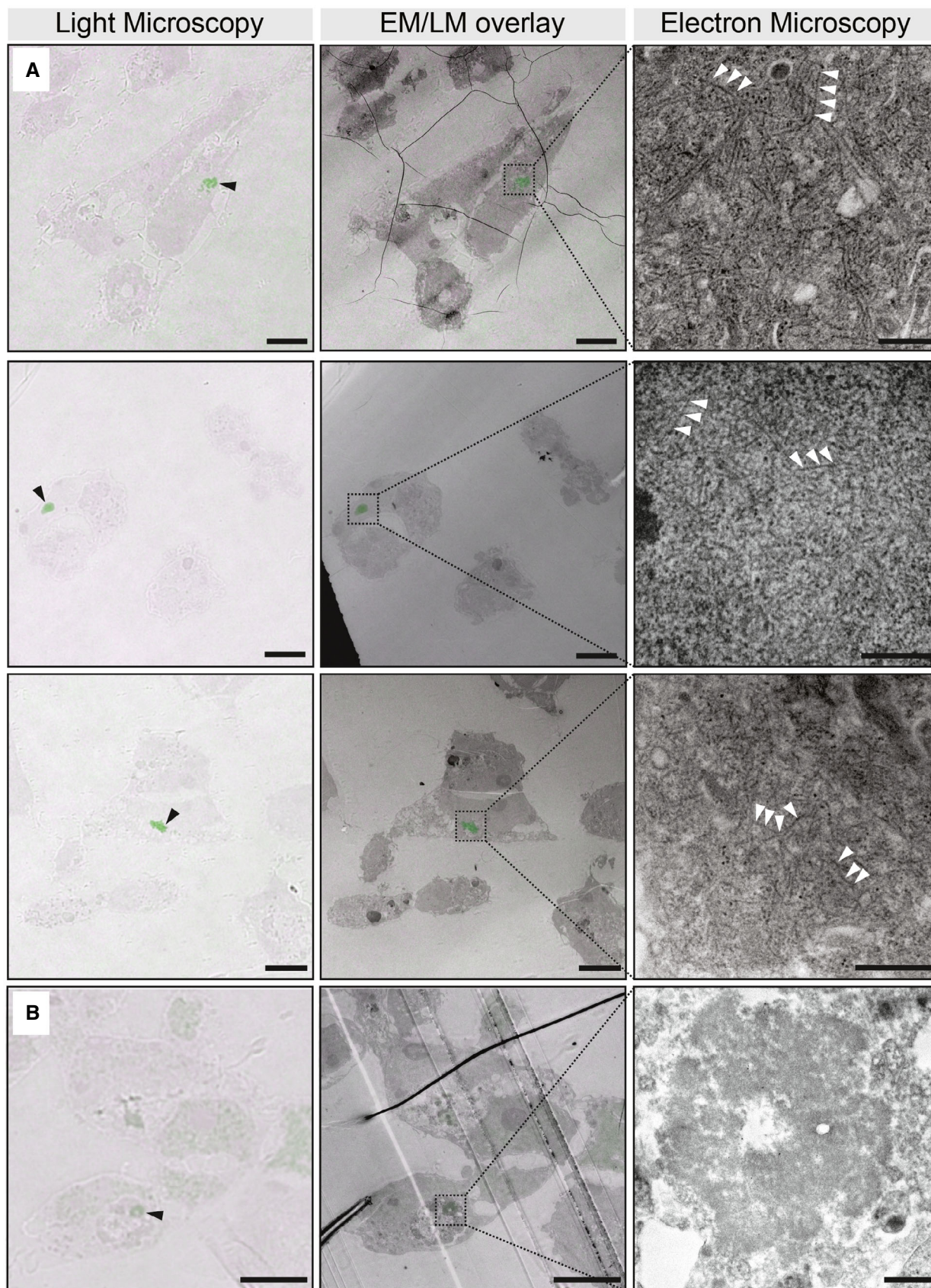
Figure 5.

To investigate the ultrastructure of the dystrophic axons, we used CLEM to localize and characterize seven TDP-43-immunopositive dystrophic axons from postmortem brain tissue of four FTLD-TDP-C donors (Figs 6D and EV5A–F). By light microscopy, for each dystrophic axon a continuous stretch of immunopositive staining spanning approximately 20 μm was visible within the same plane of a single tissue section. By EM, the ultrastructure of dystrophic axons was characterized by sparsely distributed fibrils often showing a linear arrangement and were frequently interspersed with cellular organelles and vesicles (Fig 6D and EV5A–F). Round TDP-43-immunopositive inclusions were also observed in this tissue and comprised a similar ultrastructure. By light microscopy, these round inclusions could be identified consecutively through volumes of tissue longer than the width of the inclusion, indicating that they likely represent cross-sections of the dystrophic axons (Fig 6D cross-section, Fig EV5G).

To investigate if there are differences between the nanoscale structure of fibrils observed in FTLD-TDP-A NCIs and FTLD-TDP-C dystrophic axons, we used electron tomography and subtomogram averaging. The resulting 3D averages had an optimal resolution of ˜40 Å and showed a rod-like signature typical of fibrils. However, there were no visually obvious features that differed between the two subtypes (Fig 6E). The average fibril diameter from all FTLD-TDP-A aggregates measured 7.8 nm ± 1.1, compared to an average fibril diameter of 7.5 nm ± 1.3 calculated for FTLD-TDP-C aggregates (Fig 6F). Even though there was no statistically significant difference in the fibril diameter between the two subtypes, there was higher variability in fibril width across FTLD-TDP-C patient samples. This observation suggests that these aggregates could be composed of heterogeneousTDP-43 fibrils and/or the presence of intermixed cytoskeletal filaments in comparison to a more homogeneous fibril composition for FTLD-TDP-A. To confirm that morphological features would be detectable within chemically fixed and resin-embedded postmortem brain samples, we compared the subtomogram averages of the TDP-43 fibrils to that of cytoskeletal filaments observed within the same tissue. In contrast to the TDP-43 fibrils, the resulting 3D averages of these filaments showed a discernible twist and had a diameter of 5.2 nm ± 1.7 (Fig 6E and F).

Importantly, FTLD-TDP-A fibrils appeared more densely packed compared to fibrils from FTLD-TDP-C patient samples (Fig 6B and D). We measured the density of fibrils in each tomogram by calculating the minimum distance between the backbones of adjacent fibrils. Confirming our qualitative observations, the average distances between adjacent fibrils in each aggregate was significantly lower for FTLD-TDP-A than FTLD-TDP-C (Fig 6G). Additionally, the data showed much higher variance in the average distance between FTLD-TDP-C compared to FTLD-TDP-A fibrils, consistent with a more homogeneous fibril composition for FTLD-TDP-A.

Discussion

FTLD subtypes display heterogeneity in the morphology of TDP-43 pathology and clinical manifestation of the disease, yet little is known about the mechanisms driving these differences. Patients with FTLD-TDP-C pathology have significantly longer disease duration compared to FTLD-TDP-A (Lee et al, 2017; Laferrière et al, 2019), which is a more aggressive subtype of the disease. In this study, we investigated the potency of pathological TDP-43 seeds extracted from postmortem brain tissue to induce *de novo* aggregation in HEK cells. Our results demonstrated that FTLD-TDP-A and FTLD-TDP-C follow separate mechanisms for a template-mediated aggregation process, which may be guided by differential phosphorylation, underpinning structural polymorphism between subtype-specific fibril strains.

FTLD-TDP-A and C brain-derived aggregates exhibit distinct seeding properties

In this study, the entrance of pathological aggregates in the cells was facilitated by liposome-based transfection. For both subtypes,

---

Figure 6. Fibril organization and cellular microenvironment differentiate FTLD-TDP-A from FTLD-TDP-C aggregates in patients.

A 2D TEM (first column) shows an example of the overall morphology of neuronal cytoplasmic inclusions from FTLD-TDP-A localized in postmortem human brain by correlative light and electron microscopy (also shown in Fig EV4D). 2D projections of the central slices of reconstructed 3D tomograms (middle column) taken at higher magnification within the aggregate show a dense accumulation of filaments seemingly enclosed by a boundary membrane (white arrowheads). The positions of filaments selected for subtomogram analysis are shown within a single orthoslice from the same tomogram (colored, dots last column).

B STED imaging of nuclear structures (left column) and neuronal cytoplasmic inclusions found in a postmortem tissue of a patient with FTLD-TDP-A. LaminB1 (green) was used as a nuclear membrane marker along with TDP-43 (cyan) and TDP-43$^{pS403/404}$ (magenta).

C Confocal imaging of dystrophic neurites found in a postmortem tissue of a patient with FTLD-TDP-C. Dystrophic neurites were identified using TDP-43 (cyan), and TDP-43$^{pS403/404}$ (magenta). Neurite markers were used to visualize neuronal projections (MAP2 for dendrites, PNF for axons; yellow and orange, respectively).

D 2D TEM (first row) of dystrophic neurites from FTLD-TDP-C, localized in postmortem human brain by correlative light and electron microscopy (also shown in Fig EV5D). 2D projections of the central slices of reconstructed 3D tomograms (middle row) taken at higher magnification from regions within each aggregate show a sparse arrangement of filaments which are interspersed with vesicles (white asterisk). A similar arrangement of sparse filaments and vesicles is seen in a cross-section of a dystrophic neurite from FTLD-TDP-C (cross-section, also shown in Fig EV5G). The positions of filaments selected for subtomogram analysis are shown within a single orthoslice from the same tomogram (colored dots, last row).

E Representative 3D volumes resulting from the average of sampled filaments within tomograms are depicted for FTLD-TDP-A (FTLD-A), FTLD-TDP-C (FTLD-C) and cytoskeletal filaments (CF). No significant differences in morphology between the two FTLD subtypes were detected from the 3D averages, compared to the CFs which are visibly thinner and display a distinctive twist (dotted line).

F Average width of fibrils calculated from every particle cropped along the fibrils within each collected tomogram. The data points represent the average width calculated from the total number of particles extracted from multiple tomograms for the aggregates localized for FTLD-TDP-A (n = 5 biological replicates) and FTLD-TDP-C, CF (n = 6 biological replicates). The total number of particles extracted for each aggregate are shown in Appendix table S3. Error bars represent ± standard deviation. The total average width calculated from all fibrils from FTLD-TDP-A is 7.8 nm (± 1.1 nm), 7.5 nm (± 1.3 nm) for FTLD-TDP-C and 5.2 nm (± 1.7 nm) for CF.

G The average distance between fibrils within each aggregate for FTLD-TDP-A and FTLD-TDP-C is shown. Data points represent the total combined average for all tomograms collected within a single aggregate (n = 1 biological replicate). Error bars represent ± the maximum standard deviation for each aggregate. *P*-value calculated from an unpaired *t*-test between averages of FTLD-TDP-A and FTLD-TDP-C.
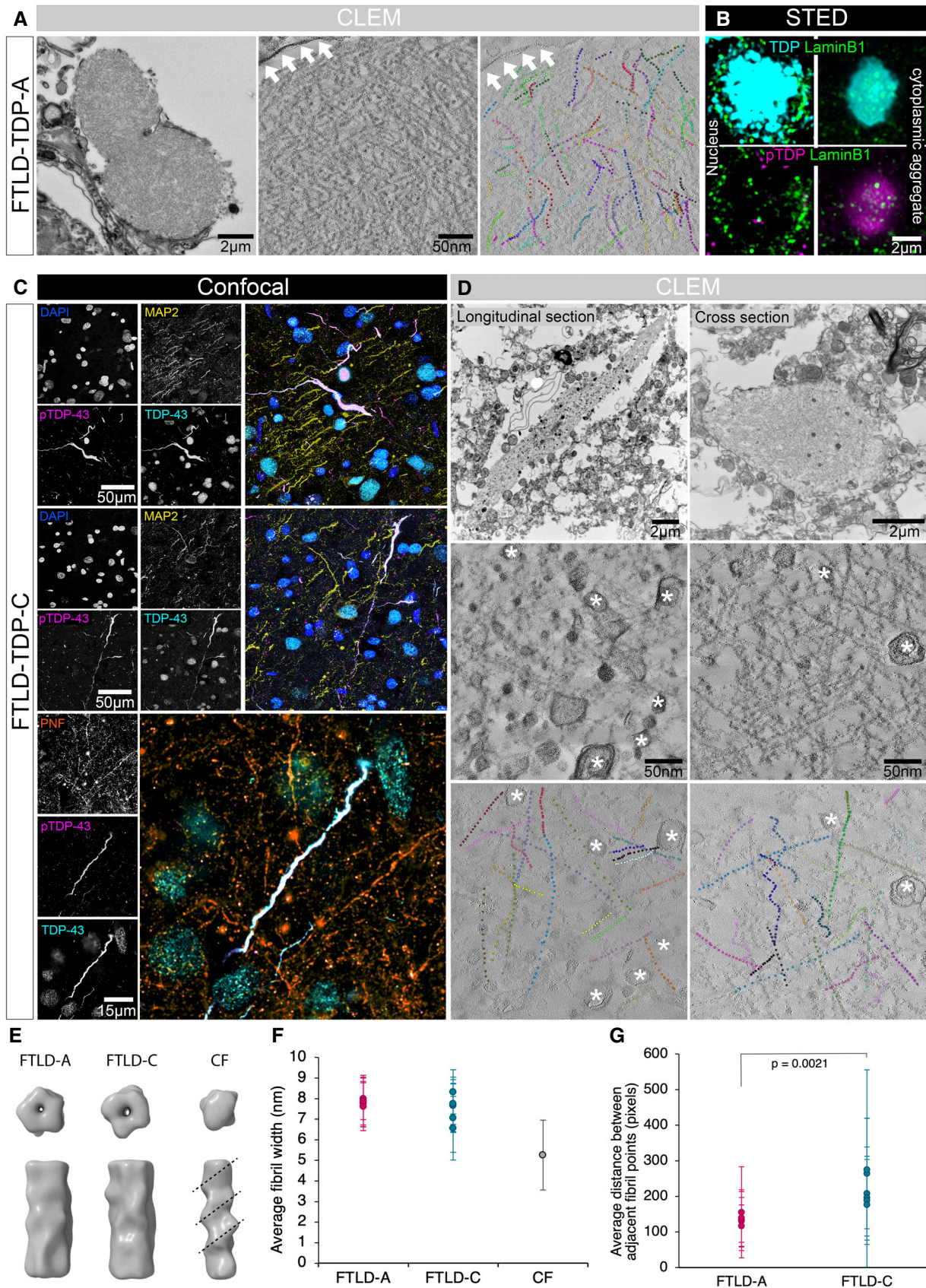
Figure 6.

the seeded cells displayed nuclear clearance of endogenous TDP-43 and cytoplasmic aggregation of phosphorylated TDP-43 (Fig 1A and B). Moreover, these cytoplasmic neoaggregates displayed properties of the original patient subtypes. Upon inoculation in cells, we found that FTLD-TDP-A seeds triggered neoaggregation more efficiently than FTLD-TDP-C, reflecting the rate of clinical disease and in line with previously published data (Laferrière et al, 2019; Porta et al, 2021). Neoaggregation was associated with nuclear clearance of TDP-43 and changes in nuclear morphology (Fig EV1A–M). We hypothesized that the loss of TDP-43 in the nucleus could lead to nuclear dysfunctions, which could be the underlying mechanism driving changes in the nuclear shape. FTLD-TDP-A neoaggregates were significantly bigger than the ones from FTLD-TDP-C (Figs EV1C, 3D, and 4E), had a higher density of accumulated TDP-43 (Fig 4G and H) and were composed of fibrils (Fig 5A), resembling the densely packed TDP-43 fibrils within NCIs in brains from patients with FTLD (Figs 6A and G, and EV4). In comparison, type C-inoculated cells contained multiple, small cytoplasmic neoaggregates (Fig 4E) which consisted of loosely packed (Fig 4G) amorphous protein with no detectable fibrils (Fig 5B). The absence of fibrils in the type C neoaggregates suggests an earlier stage in the aggregation process, in which the TDP-43-HA accumulation was initiated in the cell, but did not yet comprise any higher order structures detectable by EM.

Different rates of fibril growth point to structural polymorphism

Our results support a different rate of fibril formation in the neoaggregates, whereby cells seeded with FTLD-TDP-A patient material formed fibrils faster than FTLD-TDP-C-seeded cells. In vitro studies show that the rate of fibril growth is highly dependent on the atomic structure of the seed template (preprint: Meng et al, 2020), and that the composition of seeding material has a significant effect on the resulting fibril structure (Meier et al, 2017; Lövestam et al, 2021; Shi et al, 2021). Consistent with these studies, we saw that transfection with rec-hTDP-43 amorphous aggregates was not potent in triggering neoaggregation (Fig 2C and D). Furthermore, denaturation of the seeding material abolished the formation of intracellular neoaggregates (Fig 2A and B), supporting a template-directed amplification.

The growth rate of fibrils also depends on the heterogeneity of the seeds, where homogenous templates grow much faster than a heterogeneous mixture (Hu et al, 2017; Watanabe-Nakayama et al, 2020). Our results show that FTLD-TDP-A NCIs were more homogeneous in fibril composition compared to dystrophic neurites in FTLD-TDP-C human brain (Fig 6A, D, F and G). As intracellular fibril formation has been linked to cytotoxicity (Vasili et al, 2019), our data suggest that structural homogeneity of the seeding template confers a higher efficacy of fibril formation correlating with the more rapid clinical progression of the disease. While other factors likely play a role in the seeding efficiency of pathological TDP-43, our results suggest that the potency of intracellular TDP-43 aggregation resides in the specific structural conformation of the pathological seeds.

Therefore, it was surprising that we were unable to determine any ultrastructural differences between the fibrils in FTLD-TDP-A and FTLD-TDP-C patient brains, despite the fact that their 3D profiles were clearly distinguishable from twisted neurofilaments

(Fig 6E and F). It is possible that the fibrils comprising both subtypes of TDP-43 inclusions were morphologically too heterogeneous for the subtomogram averaging to converge on any particular feature. However, the FTLD-TDP-A homogeneous fibril composition shown by our tomographic analysis, speaks against that. Therefore, we hypothesize that any structural polymorphism between the subtypes must be driven by atomic differences in the internal structure of the fibrils, below the resolution limit achievable in chemically fixed and resin-embedded tissue samples (Lewis et al, 2019). Structural analysis of the TDP-43 fibrils with cryo-CLEM in vivo could resolve these molecular differences.

Phosphorylation guides structural polymorphism in disease subtypes

Recent studies support the notion that serine phosphorylation within the low complexity region of TDP-43 may inhibit protein aggregation in vitro and in cells. Indeed, cryo-EM studies showed that the core fibril structure would be significantly disrupted by phosphorylation at key residues in that same domain (Li et al, 2021), whereas an independent study showed that TDP-43 phosphorylation within the C-terminal region increases solubility and counteracts protein accumulation in cells (preprint: Silva et al, 2021). In combination with our results pointing to fibril structure polymorphism between the subtypes, these data suggest that the phosphorylation state of TDP-43 could play a key role in the mechanism underlying the disease-specific subtypes. Consistent with this hypothesis, we found that the seeding potency of FTLD-TDP-A extracts, but not FTLD-TDP-C, directly correlated with the TDP-43 phosphorylation level measured in the patients (Fig 1E). This result supports previous studies on postmortem brain tissue from patients with FTLD pathology, showing different levels of phosphorylation between disease subtypes (Tan et al, 2013; Laferrière et al, 2019).

In both type A and type C seeded cells, we observed a sequential phosphorylation with a specific timeline. In FTLD-TDP-A, pS403/404 occurred early on and prior to pS409/410 phosphorylation. Over time, this directionality was lost and both sites were phosphorylated independently of each other. In FTLD-TDP-C, pS403/404 was consistently a prerequisite for pS409/410, leading to a higher total percentage of bi-phosphorylated protein over time. The increased hyperphosphorylation and slower fibril growth rate we observed for FTLD-TDP-C is consistent with studies showing that phosphorylation increases solubility and decreased protein accumulation (preprint: Silva et al, 2021). As phosphorylation may affect the ultimate atomic structure of TDP-43 fibrils (Li et al, 2021), our results suggest that differential phosphorylation could mediate the formation of specific fibril strains to direct disease-subtype specificity. It remains unknown whether TDP-43 phosphorylation may inhibit fibril formation, or alter their structure in favor of a more (or less) toxic form.

Differential pathological mechanisms are involved in FTLD-TDP-A and FTLD-TDP-C

While both FTLD-TDP-A and C show aggregation of TDP-43 fibrils in the brain, we present multiple lines of evidence that different mechanisms underlie the aggregation and progression, potentially leading to the disease-specific phenotypes. In both our cellular

models (Fig 4A), and the postmortem human brain (Fig 6B), we found LaminB1 localized within the neoaggregates, suggesting a potential toxic mechanism by disorganization of the nuclear envelope, in agreement with a previous study (Chou *et al*, 2018). The absence of the nucleolus marker within the neoaggregates suggests a specific disorganization of the nuclear membrane protein complexes. This is further supported by our EM structural analysis showing membranous material encircling the NCIs in patient brains (Figs 6A and EV4).

While our data illustrate low seeding efficiency of FTLD-TDP-C-derived aggregates, a recent study did not detect any evidence of seeding in this subtype (Porta *et al*, 2021). This apparent discrepancy may be explained by the different timelines used in the two studies and the high patient-to-patient variability characterizing the FTLD-TDP-C seeds. Indeed, our results indicate that FTLD-TDP-C fibrils within dystrophic neurites are a mixture of fibrils, with high variability in width and density, and with intercalated cytoskeletal and vesicular elements, which was reflected in the propensity to seed neoaggregates, which was variable among different patient samples. We also found that FTLD-TDP-C neoaggregation formation peaked at days 5–6 post inoculation suggesting that analysis at earlier time points, that is, day 3 post incubation (Porta *et al*, 2021), might conceal the seeding effect.

Altogether, we demonstrated that FTLD patient-derived TDP-43 aggregates amplify within cells via a template-directed process. Importantly, we showed the prion-like, strain behavior of pathological TDP-43, as FTLD subtype-specific changes were found in seeding potency, neoaggregate size and structure, as well as co-aggregated proteins. Seeding of endogenous TDP-43 was accompanied by its progressive nuclear clearance overtime and triggered measurable toxicity in a subtype-specific manner that correlates with progression rates of the disease subtypes in patients. We additionally showed that phosphorylation of the low complexity region of TDP-43 - a pathognomonic mark for TDP-43 proteinopathies - occurs in a sequential N-to-C-terminal fashion and that it is distinct in the different subtypes, suggesting that phosphorylation impacts fibril formation. These models will be helpful in identifying regulators of TDP-43 phosphorylation, fibrillization, aggregation, and mislocalization. Moreover, they can be used to test potential therapeutics targeting TDP-43 nuclear clearance and aggregation in order to slow down or stop disease progression.

Materials and Methods

Postmortem brain tissue

All patient samples were received from the Queen Square Brain Bank (QSBB) for Neurological Disorders, at University College of London (UCL) and the Netherland Brain Bank (NBB) at the Netherlands Institute for Neuroscience, Amsterdam (Appendix Table S1). All material has been collected from donors for or from whom a written informed consent for a brain autopsy and the use of the material and clinical information for research purposes had been obtained by the NBB or QSBB. Patient identity was anonymized by QSBB and NBB before shipment to the University of Zurich (UZH). Frozen blocks of brain tissue were used in this study. All samples were fixed in 3.65% formalin at autopsy and either processed

directly for EM or post-fixed in 0.1% glutaraldehyde before processing for EM.

Homogenization of brain tissue

Homogenization was performed as previously described (Laferrière *et al*, 2019; Pérez-Berlanga *et al*, 2019). The samples were stored at −80°C and transported on dry ice to avoid thawing of the tissue. For homogenization, the brain tissue was cut in a piece of approximately 300 mg with a sterile razor and placed into a 2-ml tube containing a mixture of ceramic beads with a diameter of 1.4 and 2.8 mm (Precellys, P000918LYSK0-A). 1X homogenization-solubilization buffer (10 mM Tris-HCl pH 7.4, 150 mM of NaCl, 0.5 mM of EDTA, 1 mM of Dithiotreitol, complete EDTA-free protease inhibitors (Roche), PhosSTOP phosphatase inhibitors (Roche)) was added in a ratio of 5:1 to the amount of tissue for a final concentration of 20%. The samples were then homogenized with a Minilys device (Bertin, P000673-MLYS0-A) or Precellys homogenizer (P000062-PEVO0-A) in three rounds for each 30 s, while cooling the samples on ice between the rounds. After homogenization, aliquots of 150 µl were produced in protein low-binding 1.5-ml tubes (Eppendorf, 0030108116). The aliquots were shock-frozen in dry ice and placed back into the −80°C freezer.

SarkoSpin on brain homogenates

SarkoSpin was performed as previously described (Laferrière *et al*, 2019; Pérez-Berlanga *et al*, 2019). Fifty microliters of Benzonase mix, containing 14 mM of $MgCl_2$ and 250 U benzonase (Merck Millipore, 71205-3) in 1× HS buffer was added to 150 µl of brain homogenate. After 5 min incubation at room temperature, 200 µl of 4% N-lauroyl-sarcosine (sarkosyl, Sigma, 61739) in 2× HS buffer (20 mM of Tris-HCl pH 7.4, 300 mM of NaCl, 1 mM of EDTA, 2 mM of Dithiotreitol, complete EDTA-free protease inhibitors (Roche), PhosSTOP phosphatase inhibitors (Roche)) was added to each sample. For solubilization, the samples were put on a heating block (Thermomixer, Eppendorf) for 45 min at 38°C at 600 rpm. Afterward, 200 µl of 0.5% sarkosyl in 1× HS buffer was added per sample and was centrifuged at 21,200 *g* for 30 min at room temperature. The supernatant was discarded, and the pellet was cleaned twice with 100 µl of phosphate-buffered saline (Gibco, 10010015) to carefully remove lipids from the pellet. The pellet was then resuspended in 200 µl of phosphate-buffered saline (PBS, Gibco 10010015) for seeding on HEK cells by sonication (Qsonica, Q2000) with an amplitude of 60% power and 3 s on/3 s off for 3 min. The sample was used fresh to seed on cells.

Protein expression and purification

The expression of recombinant human TDP-43 with an additional C-terminal Maltose-binding protein and a C-terminal His_6-tag was done using the pJ4M expression vector from addgene. Protein production was done in One Shot™ BL21 Star™ (DE3) chemically competent *Escherichia coli* cells (Life Technologies). Bacterial culture induction was performed at an $OD_{600} = 0.8$ through addition of 1 mM of isopropyl β-D-thiogalactoside (IPTG) at 16°C for 20 h in Luria-Bertani (LB) medium. After cell harvesting (Sorvall SLA-3000, 5,000 *g*, 4°C, 20 min), the palettes were resuspended in 60 ml of

lysis buffer (20 mM of Tris-HCl, pH 8.0, 1 M of NaCl, 10 mM of imidazole, 10% glycerol, 1 mM of Tris-(2-carboxyethyl)-phosphine Hydrochloride (TCEP), 10 EDTA free mini protease inhibitors) for 2 l of bacterial culture. Cell lysis was performed by sonication (W-385 LSL SECFROID Sonicator, Heat System Ultrasonic, 11 cycles, 10 s on, 20 s off). The cell lysate was centrifuged (Sorvall SS-34 rotor, 15,000 g, 4°C, 20 min) and the supernatant was applied on 15 ml of Ni-Sepharose excel column material (GE Healthcare) packed in a glass gravity column (Econo-Column® Chromatography Columns, 2.5 × 30 cm, Bio-Rad Laboratories AG), which had been equilibrated before usage (30 mM of Tris-HCl, pH 8.0, 150 mM of NaCl, 10% Glycerol, 1 mM of Dithiothreitol (DTT)). A first wash was performed with 40 ml of lysis buffer and a second wash with 50 ml of wash buffer (30 mM of Tris-HCl, pH 8.0, 3 M of NaCl, 10% Glycerol, 1 mM of DTT). Elution was achieved by applying 30 ml of elution buffer (20 mM of Tris-HCl, pH 8.0, 1 M NaCl, 10% Glycerol, 500 mM imidazole, 1 mM TCEP). The protein was concentrated using pre-equilibrated Amicon 10,000 MWCO 15 ml concentrator (Merck). Up to 10 ml of concentrated protein was injected onto a Hiload 26/60 Superdex size-exclusion chromatography (SEC, GE Healthcare) column connected to an ÄKTA Pure system (Cytavia). The SEC was run with a flow rate of 1 ml/min in SEC buffer (20 mM Tris-HCl, pH 8.0, 300 mM NaCl, 1 mM TCEP, 0.0007% Tween-20). Pure eluted 1 ml fractions (analyzed by LDS polyacrylamide gel electrophoresis and silver staining) were concentrated with Amicon 10,000 MWCO 15-ml concentrators (Merck), flash frozen and kept at −20°C.

Preparation of rec-hTDP-43 aggregates

Purified recombinant TDP-43-MBP was thawed on ice and buffer exchanged into aggregation buffer (50 mM Tris-HCl, pH 7.4, 200 mM Trehalose, 100 mM of potassium acetate, 0.5 mM EGTA, 20 mM Glutathione) using Amicon Ultra-0.5 Centrifugal Filter Units. 5 μM FL-TDP-43-MBP was incubated with TEV protease for 18 h at 25°C without agitation. Recombinant TDP-43 aggregates were collected by centrifugation at 15,000 g for 30 min. The supernatant was discarded, the aggregates were resuspended in PBS by sonication (Qsonica, Q2000) with an amplitude of 60% power and 3 s on/ 3 s off for 3 min and immediately seeded on HEK 293T cells.

Seeding SarkoSpin pellet or rec-hTDP-43 on HEK cells

HEK293T Flp-In-T-REx (Invitrogen) cells expressing TDP-43-HA under doxycycline (dox, Clontech, 631311) induction were generated as described in Laferrière et al, 2019. HEK293T cells were cultured in Dulbecco's Modified Eagle's medium (DMEM, Sigma D5671), supplemented with 10% fetal calf serum (FBS, Life Technologies A3160802), 1× GlutaMAX (Gibco 35050038), 1× penicillin-streptomycin (Sigma P4333), 0.2% hygromycin (Invitrogen 10687010) and 0.04% blasticidin (Invitrogen 4069-ant-bl-10p), and maintained in incubators at 37°C and 5% CO$_2$. Plates were coated with 100 μg/ml Poly-D-Lysine Hydrobromide (PDL) and incubated at 37°C for at least 1 h. HEK293 cells were plated at 225 cells/mm^2. After one day, TDP-43-HA was induced by adding dox in a ratio of 1:500 in the HEK stable medium. One day later, the SarkoSpin protocol was performed (Laferrière *et al*, 2019). For rec-hTDP-43 seeding, the aggregates were prepared as described in *Preparation of*

rec-hTDP-43 aggregates. The SarkoSpin pellet or the rec-hTDP-43 aggregates were prepared for seeding by incubating it with OptiMEM and Lipofectamine2000 (ratio 1:2.5 ~ SarkoSpin pellet to Lipofectamine) for 30 min. 0.05 μg sarkospin pellet was added for 1 mm^2 coverslip. After incubation of 3–4 h, HEK media containing 20 nM of AraC and dox (1:500) was added. One day after seeding, the media was exchanged to HEK media containing 20 nM of AraC and dox (1:500).

Fixation of seeded HEK cells, staining and mounting of samples

At specific time points, the wells were first washed once with PBS and then fixed for 30 min with a 4% PFA and 4% sucrose solution. After fixation, the plates were again washed once with PBS and stored in fresh PBS at 4°C. PBS was removed from the wells and a 50 mM NH$_4$Cl in PBS with 0.25% Triton solution was incubated for 1 h, to quench autofluorescence. After removing of the quenching solution, the primary antibody in saturation buffer (10% donkey serum, 3% BSA and 0.25% Triton in PBS) was added and incubated overnight at 4°C. The next day, the plates were put at room temperature for 1 h to let them warm up gently. Then, the wells were washed three times with PBS before the secondary antibody in saturation buffer was added. After incubation for 2–3 h in the dark at room temperature, the plates were washed three times with PBS. The staining was stabilized by adding 4% PFA, 4% sucrose in PBS solution for 5 min. After another three washes with PBS, DAPI was stained for 30 min in the dark at room temperature. The plates were washed another three times and then placed back in the 4°C fridge. Coverslips were mounted with Prolong Diamond Antifade Mountant (Invitrogen, P36961). Antibodies used can be found in Appendix Table S2. All secondary antibodies were purchased from Thermo Fisher Scientific.

Confocal microscopy and image processing to count neoaggregates

Confocal LM images were taken with a Leica Falcon SP8 at the Center for Microscopy and Image Analysis (ZMB) at the University of Zurich. Images were acquired using HC PL APO corr CS2 20× objective (NA 0.75) at a 2,048 × 2,048 pixels resolution achieving 227 nm pixel resolution. Microscope parameters were kept constant between conditions and experiments. Three independent experiments were imaged with seven control, seven FTLD-TDP-A and six FTLD-TDP-C cases. The images were deconvoluted with Huygens and processed with Imaris Version 9.3 by reconstructing the image using surfaces (Appendix Fig S1A). Surface parameters were created by choosing an intensity and size threshold for DAPI, nuclear TDP-43-HA, aggregated TDP-43-HA and phosphorylated TDP-43. For TDP-43-HA, the same intensity threshold but different size parameters were applied to distinguish between nuclear (volume above 235 μm^3) and aggregated TDP-43-HA (area between 1.25 and 234 μm^2). The same size parameter used for aggregated TDP-43-HA (area between 1.25 and 234 μm^2) was applied to phosphorylated TDP-43. Number of voxels was fixed to be above 10.0 for all surfaces, except for the surface of DAPI where it was fixed at 2,500. Grain size of the surface for DAPI was fixed at 0.5 μm, for nuclear TDP-43-HA at 0.4 μm and for aggregated TDP-43-HA and phosphorylated TDP-43 at 0.2 μm. Surface to surface colocalization between DAPI and

nuclear TDP-43-HA and between aggregated TDP-43-HA and phosphorylated TDP-43 was determined. Colocalization surface of the surfaces DAPI and nuclear TDP-43-HA was smoothed with a grain size of 0.454 whereas the colocalization surface of the surfaces aggregated TDP-43-HA and phosphorylated TDP-43 was not smoothed. To visualize mask images and for distance calculations, Imaris Version 9.6 was used. Distances between each neoaggregate and phosphorylated neoaggregate to DAPI and colocalization of DAPI and nuclear TDP-43-HA were calculated by using the corresponding surfaces created.

Confocal microscopy and image processing to measure phosphorylated TDP-43

Confocal LM images were taken using Leica Falcon SP8 at the ZMB at the University of Zurich. Images were acquired with the 63× objective HC PL APO corr CS2 (NA 1.4) at 2,048 × 2,048 pixels resolution, achieving 72 nm pixel resolution. Microscopy settings were kept constant between the conditions during the imaging. The images were analyzed using Fiji Software 1.8.0 172 by applying a mask to the image with a constant threshold (DAPI: 12,000, pTDP-43 200,000). The area was measured for each channel and the pTDP-43 area was normalized to the DAPI area per image.

Overexpression of GFP-TDP-43 mutants in NSC-34 cells

Plates were coated with 1:60 Matrigel (Corning, 8015325) for at least 1 h at 37°C. NSC-34 cells were thawed and plated at 315 cells/mm^2 (300,000 cells per well in a 6-well plate). Cells were cultured in NSC-34 media (DMEM-F-12, B27+ (2×), N2 (1×), Glutamax (1×), Pen/Strep (0.2×), BDNF (1:1,000) and GDNF (1:1,000)). When the cells reached a confluency of 80–85%, they were transfected with the different GFP-TDP-43 mutants. 2,000 ng DNA was added to 190 μl of OptiMEM and 8 μl of Lipofectamine2000 was added to another 190 μl of OptiMEM. The two preparations were mixed and incubated for 20 min at RT. 450 μl of media was added and the total 830 μl per well was put on the cells. After 3 h incubation at 37°C, additional 400 μl of media was added per well. 24 h after transfection, the media was changed (2.5 ml of fresh NSC-34 media per well). 48 h after transfection, the cells were snap-frozen on dry-ice and the plates were stored at −80°C. To prepare the samples for western blot, cells were lysed in RIPA buffer (10 mM Tris-Cl (pH 8.0), 1% Triton X-100, 0.1% sodium deoxycholate, 0.1% SDS, 140 mM NaCl, 1.5 mM MgCl$_2$, supplemented with 1 tablet Complete Mini EDTA-free protease inhibitor (Roche, 11836170001) and 1 tablet PhosSTOP (Roche, 04906845001)).

Western blot of NSC-34 overexpressing GFP-TDP-43 mutants

Protein concentration was measured using BCA protein assay according to manufacturer's instructions (Pierce, 23227). The same amount of protein was used for further steps. Samples were prepared by adding 1× Bolt™ LDS Sample Buffer (Invitrogen, B0008) and 1× Bolt™ Sample Reducing Agent (Invitrogen, B0009) and denatured for 10 min at 90°C. Samples were loaded along a protein ladder (Thermofisher, 26616) on a 4–12% Bis-Tris gel (Life Technology, NW04125BOX). The gel was run for 10 min at 80 V and then for approximately 45 min at 120 V. Transfer was done using iBlot2 gel transfer device (Life Technology, IB21001) with a 7 min transfer program at 70 V on a PVDF membrane (Life Technology, IB24001). The membranes were blocked for 1–1.5 h in 5% milk in PBS-Tween20 (PBS-T, PBS containing 0.025% Tween-20, Sigma, P1379). To achieve clean blots for pTDP-43 antibody, the membranes were washed three times 10 min with PBS-T. After washing, primary antibody (Appendix Table S2) was added either in 5% milk (total TDP-43 antibody) or in 2.5% bovine serum albumin (BSA, Sigma, A4503) in PBS-T and the membranes were incubated overnight at 4°C. The next day, membranes were washed three times for 10 min with PBS-T before incubating for 45 min at RT with the secondary antibody in either 5% milk (total TDP-43 primary antibody) or 2.5% BSA (pTDP-43 antibody). After three washes with PBS-T, the membranes were imaged with Fusion FX imager (Vilber).

Superresolution optical microscopy (STORM)

HEK cells were transfected with patient derived TDP-43 seeds as described above and fixed 6 days after transfections. Cells were fixed and stained as described above. Images were acquired using a Widefield/TIRF – Leica SR GSD 3D LM at the ZMB at the University of Zurich, using an HCX PL APO 160× objective (NA 1.43) and using GSD mode of the Leica X software suite. Images of the 647 nm channel were acquired using a 642 nm laser, of the 568 nm channel were acquired using a 532 nm laser, and of the 488 nm channel using a 488 nm laser. To achieve ground state depletion of the aggregates, pumping was performed with 100% laser power (for channel 568 and 647) for 5–10 min. Particles were then acquired using laser power of 10% over 100,000 frames. No UV back-pumping was used for 568 and 647 channels to ensure stoichiometric measurement of the particle density. Cells were blindly selected using cellular marker stainings. Aggregates were imaged in the same condition for type A and type C. Images were then processed as previously described in (De Rossi *et al*, 2020) using Fiji plugin ThunderSTORM. Processing was performed as suggested from the ThunderSTORM user's guide, using Wavelet filter B-spline (B-spline order: 3, scale 2.0), molecules localization was approximated using local maximum method with a peak intensity threshold at 1.5*std (Wave.F1). Subpixel localization was performed using PSD integrated Gaussian methods with a fitting radius of 5 and initial sigma 1.6 using weighted least squares fitting method. Images were then filtered using Sigma plot to remove grid artifacts. Number of particles per aggregate was extracted using ROI filtering. Area of the aggregates was measured in image J using thresholding method. Data were extracted as CSV files.

Confocal and Stimulated emission depletion (STED) imaging of human brain

For confocal images, images were acquired using Leica Falcon SP8 at the ZMB at the University of Zurich. Images were acquired with the 63× objective HC PL APO corr CS2 (NA 1.4) at 2,048 × 2,048 pixels resolution, achieving 72 nm pixel resolution. Huygens professional was used for deconvolution and Fiji was used for analysis and rendering. Super-resolution STED (Stimulated emission depletion microscopy) was acquired with a Leica SP8 3D, 3-color gated STED laser scanning confocal microscope. A 775-nm depletion laser

was used to deplete both 647 and 594 dyes. The powers used for depletion lasers, the excitation laser parameters, and the gating parameters necessary to obtain STED resolution were assessed for each marker. Z-stacks of 1,504 × 1,504-pixel images at 40 nm step size were acquired at 1,800 kHz bidirectional scan rate using a × 100 (1.45) objective with a digital zoom factor yielding 25.23 nm pixels resolution.

Correlative light and electron microscopy (CLEM)

For CLEM, samples were prepared as described in (Shahmoradian et al, 2019). Briefly, formalin fixed, postmortem human brain tissue samples were post-fixed in 0.1% glutaraldehyde and cut into 60 μm sections with a vibratome (VT1000 S, Leica Biosystems). The sections were further fixed in osmium tetroxide reduced with potassium ferrocyanide, followed by a second incubation with aqueous osmium tetroxide and staining with uranyl acetate at 4°C overnight. Sections were then stained with lead aspartate solution at 60°C, dehydrated in a graded ethanol series on ice, and embedded in Durcupan resin. Fixed FTLD-seeded cells (4% paraformaldehyde, 0.1% glutaraldehyde) were washed in 0.1 M sodium cacodylate, stained with 1% osmium tetroxide for 30 min and 1% uranyl acetate 20 min, dehydrated in a graded ethanol series and embedded in Embed 812 resin (EMS). Serial ultrathin sections (150 nm) of resin-embedded samples were generated using an ultramicrotome (Ultracut EM UC7, Leica Biosystems) and alternately collected on Superfrost Plus glass slides (Thermo Fisher Scientific) for later light microscopy and electron microscopy grids coated with a carbon-stabilized formvar film (EMS Diasum) for EM imaging.

Light microscopy

Slides were processed for immunohistochemistry LM as follows: The sections were etched in a saturated ethanolic potassium hydroxide solution for 3 min followed by washing in PBS. For brain sections, endogenous peroxides were quenched with 1% hydrogen peroxide in 10% methanol for 10 min followed by blocking in antibody diluent (Dako/S202230) for 10 min. The sections were incubated in primary antibody (TDP43 3H8, Novus Biologicals, 1/1,000 dilution) for 1 h at 37°C followed by washing with 0.25% Triton X-100 in PBS and incubation with the Immpress reagent anti-mouse IgG conjugated to horseradish peroxidase (Reactolab) secondary antibody for 30 min at room temperature. For FTLD-seeded cells, antigen retrieval was performed by incubation in 95% formic acid for 10 min and heat-treatment at 95°C in Tris-EDTA pH 9.0 for 30 min. Endogenous peroxidases were quenched as above followed by incubation with primary antibody (anti-HA, 1/1,000 dilution) overnight at 4°C and Immpress anti-rabbit IgG conjugated to horseradish peroxidase (Reactolab) for 30 min at room temperature. Bound antibody complexes were detected using the Permanent HRP Green Kit (Zytomed Systems) with incubation for 3 min at room temperature, before counterstaining with hematoxylin, dehydration and coverslipping. The slides were screened by light microscopy to identify TDP-43 pathology/HA immunopositive cellular inclusions. Images of slides displaying immunopositive inclusions were collected at 60× magnification using a Nikon Ti-E widefield equipped with a color camera, or at 63× magnification using a Leica DMi8 equipped with a DMC4500 color camera. Images were

adjusted for contrast in Fiji (Schindelin et al, 2012) where necessary and color-blind corrected by replacing the red channel with magenta.

Electron microscopy

Transmission electron microscopy (TEM) images of electron microscopy grids containing sections immediately adjacent to those on the selected light microscopy slides, were collected at 80 keV on a Tecnai G2 Spirit (FEI, Thermo Fisher Scientific) equipped with an Morada G3 camera (EMSIS GmbH) or a CM100 Biotwin (Philips) equipped with a TVIPS F416 camera. The resulting EM images were overlaid with the corresponding LM images, to define the specific location of the immunopositive inclusions in the EM images and guide the collection of subsequent higher resolution images and electron tomography. Images were adjusted for contrast in Fiji (Schindelin et al, 2012) where necessary.

Electron tomography

EM tomograms were collected at room temperature on a Talos F200C (FEI, Thermo Fisher Scientific) EM, operated at 200 kV and equipped with a Ceta CMOS camera (FEI). Tilt series were recorded using the SerialEM software (Mastronarde, 2005) with a pixel size of 0.32 nm, a unidirectional tilt scheme at 3° increments over a range from −60° to 60°, and a nominal defocus of −6 μm. Tilt series alignment by cross-correlation and patch-tracking followed by 3D reconstruction of unbinned tomograms were performed using etomo from the IMOD software (Kremer et al, 1996). A total number of tomograms collected for each aggregate within each patient are listed in Appendix Table S3. 2D projections of tomograms were created by averaging the central 20 slices of the tomograms using the trimvol and avgstack functions in IMOD.

Subtomogram averaging and analysis of fibrils

Sub-tomogram analysis was carried out using the Dynamo software (Castaño-Díez et al, 2012, 2017). For each tomogram, all visible fibrils were defined as individual filament models (function: crop along axis). The beginning and end of each fibril was manually defined and extracted within a plane, where the center of the fibril was defined by clicking along the horizontal fibril axis. The models were cropped using the step-by-step workflow, cropping particles every 60 pixels (dz) with a side length of 128 pixels. The particles from all tomograms taken within a single aggregate were combined for the particle alignment and subtomogram averaging. A total number of particles cropped for each aggregate are listed in Appendix Table S3. An initial particle alignment was carried out using numerical parameters outlined in Appendix Table S4. The resulting average was used as a template for refinement. Three rounds of refinement were carried out with a cylindrical mask (40 pixels). The resolution was calculated using gold standard methodology and used for bandpass filtering of the final maps. Resulting 3D averages were visualized in Chimera (Pettersen et al, 2004). A set of scripts and functions that combine Dynamo commands with standard Matlab commands were used to automatically measure the diameter and the density of the fibrils. The diameter of the particles was measured by radially averaging a 2D projection of the particles

along their main axis. The x value at the local maximum of the resulting 1D profile was chosen to be the radius of the particle, which consistently matched the visual perception of the radius. The distance between adjacent fibrils was measured by calculating the minimum distance from equidistant coordinates along each fibril to equidistant coordinates along adjacent fibrils. The combined mean and standard deviation of all these minimum distances from all tomograms of each aggregate is reported.

Graphs and statistical analysis

Schematic representations were created using BioRender (Figs 2A and EV1A, G and K). Figure 3F was created using pyMOL Molecular Graphic Systems Version 2.3.5 and phosphorylation sites were created using PyTM (Warnecke *et al*, 2014). Graphical representations were created and statistical analysis was performed using Graphpad Prism Version 9.2.

Data availability

No primary datasets have been generated and deposited.

Expanded View for this article is available online.

Author contributions

Conceptualization of the study was carried out by PDR, AJL, HS and MP. PDR, JF and LDV performed seeding experiments and phosphorylation timeline experiments, confocal image acquisition and processing, image analyses and quantification with Imaris. PDR, JF, LDV, VIW, TD and WZ performed the template denaturation seeding experiment. JF, TD, CS, and AZ performed seeding with rec-hTDP-43. JF, JW and ZG performed NSC-34 overexpression experiments. PDR performed dSTORM imaging and analysis of the cellular model and confocal and STED imaging of postmortem human samples. AJL, CB and MDF performed CLEM experiments. AJL performed tomography. AJL, SS and DC-D carried out subtomogram averaging and analysis. AA-A performed preliminary cryo-EM experiments. TL provided autopsy material and associated clinical and neuropathological information and critical input on the study.

PDR, JF and AJL prepared the figures. PDR, AJL, JF, HS and MP wrote and edited the manuscript. MP directed the entire study. All authors read, and approved the final manuscript.

Conflict of interest

The authors declare that they have no conflict of interest.

References

Afroz T, Hock E-M, Ernst P, Foglieni C, Jambeau M, Gilhespy LAB, Laferriere F, Maniecka Z, Plückthun A, Mittl P *et al* (2017) Functional and dynamic polymerization of the ALS-linked protein TDP-43 antagonizes its pathologic aggregation. *Nat Commun* 8: 45

Aguzzi A, Polymenidou M (2004) Mammalian prion biology. *Cell* 116: 313 – 327

Alami N, Smith R, Carrasco M, Williams L, Winborn C, Han S, Kiskinis E, Winborn B, Freibaum B, Kanagaraj A *et al* (2014) Axonal transport of TDP-43 mRNA granules is impaired by ALS-causing mutations. *Neuron* 81: 536 – 543

Arai T, Hasegawa M, Akiyama H, Ikeda K, Nonaka T, Mori H, Mann D, Tsuchiya K, Yoshida M, Hashizume Y *et al* (2006) TDP-43 is a component of ubiquitin-positive tau-negative inclusions in frontotemporal lobar degeneration and amyotrophic lateral sclerosis. *Biochem Biophys Res Commun* 351: 602 – 611

Ayala YM, Zago P, D'Ambrogio A, Xu Y-F, Petrucelli L, Buratti E, Baralle FE (2008) Structural determinants of the cellular localization and shuttling of TDP-43. *J Cell Sci* 121: 3778 – 3785

Babinchak WM, Haider R, Dumm BK, Sarkar P, Surewicz K, Choi J-K, Surewicz WK (2019) The role of liquid–liquid phase separation in aggregation of the TDP-43 low-complexity domain. *J Biol Chem* 294: 6306 – 6317

Bhopatkar AA, Uversky VN, Rangachari V (2020) Granulins modulate liquid–liquid phase separation and aggregation of the prion-like C-terminal domain of the neurodegeneration-associated protein TDP-43. *J Biol Chem* 295: 2506 – 2519

Brady OA, Meng P, Zheng Y, Mao Y, Hu F (2011) Regulation of TDP-43 aggregation by phosphorylation andp62/SQSTM1. *J Neurochem* 116: 248 – 259

Brettschneider J, Del Tredici K, Toledo JB, Robinson JL, Irwin DJ, Grossman M, Suh EunRan, Van Deerlin VM, Wood EM, Baek Y *et al* (2013) Stages of pTDP-43 pathology in amyotrophic lateral sclerosis. *Ann Neurol* 74: 20 – 38

Cao Q, Boyer DR, Sawaya MR, Ge P, Eisenberg DS (2019) Cryo-EM structures of four polymorphic TDP-43 amyloid cores. *Nat Struct Mol Biol* 26: 619 – 627

Castaño-Díez D, Kudryashev M, Arheit M, Stahlberg H (2012) Dynamo: a flexible, user-friendly development tool for subtomogram averaging of cryo-EM data in high-performance computing environments. *J Struct Biol* 178: 139 – 151

Castaño-Díez D, Kudryashev M, Stahlberg H (2017) Dynamo catalogue: geometrical tools and data management for particle picking in subtomogram averaging of cryo-electron tomograms. *J Struct Biol* 197: 135 – 144

Chou C-C, Zhang YI, Umoh ME, Vaughan SW, Lorenzini I, Liu F, Sayegh M, Donlin-Asp PG, Chen YH, Duong DM *et al* (2018) TDP-43 pathology disrupts nuclear pore complexes and nucleocytoplasmic transport in ALS/FTD. *Nat Neurosci* 21: 228 – 239

De Rossi P, Nomura T, Andrew RJ, Masse NY, Sampathkumar V, Musial TF, Sudwarts A, Recupero AJ, Le Metayer T, Hansen MT *et al* (2020) Neuronal BIN1 regulates presynaptic neurotransmitter release and memory consolidation. *Cell Rep* 30: 3520–3535

Feiler MS, Strobel B, Freischmidt A, Helferich AM, Kappel J, Brewer BM, Li D, Thal DR, Walther P, Ludolph AC *et al* (2015) TDP-43 is intercellularly transmitted across axon terminals. *J Cell Biol* 211: 897–911

Gasset-Rosa F, Lu S, Yu H, Chen C, Melamed Z, Guo L, Shorter J, Da Cruz S, Cleveland DW (2019) Cytoplasmic TDP-43 de-mixing independent of stress granules drives inhibition of nuclear import, loss of nuclear TDP-43, and cell death. *Neuron* 102: 339–357

Guo L, Kim HJ, Wang H, Monaghan J, Freyermuth F, Sung JC, O'Donovan K, Fare CM, Diaz Z, Singh N *et al* (2018) Nuclear-import receptors reverse aberrant phase transitions of RNA-binding proteins with prion-like domains. *Cell* 173: 677–692

Harvey RJ (2003) The prevalence and causes of dementia in people under the age of 65 years. *J Neurol Neurosurg Psychiatry* 74: 1206–1209

Hasegawa M, Arai T, Nonaka T, Kametani F, Yoshida M, Hashizume Y, Beach TG, Buratti E, Baralle F, Morita M *et al* (2008) Phosphorylated TDP-43 in frontotemporal lobar degeneration and amyotrophic lateral sclerosis. *Ann Neurol* 64: 60–70

Hu R, Ren B, Zhang M, Chen H, Liu Y, Liu L, Gong X, Jiang B, Ma J, Zheng J (2017) Seed-induced heterogeneous cross-seeding self-assembly of human and rat islet polypeptides. *ACS Omega* 2: 784–792

Inukai Y, Nonaka T, Arai T, Yoshida M, Hashizume Y, Beach TG, Buratti E, Baralle FE, Akiyama H, Hisanaga S-I *et al* (2008) Abnormal phosphorylation of Ser409/410 of TDP-43 in FTLD-U and ALS. *FEBS Lett* 582: 2899–2904

Kametani F, Obi T, Shishido T, Akatsu H, Murayama S, Saito Y, Yoshida M, Hasegawa M (2016) Mass spectrometric analysis of accumulated TDP-43 in amyotrophic lateral sclerosis brains. *Sci Rep* 6: 23281

Kim KY, Lee H-W, Shim Y, Mook-Jung I, Jeon GS, Sung J-J (2015) A phosphomimetic mutant TDP-43 (S409/410E) induces Drosha instability and cytotoxicity in Neuro 2A cells. *Biochem Biophys Res Commun* 464: 236–243

Klim JR, Williams LA, Limone F, Guerra San Juan I, Davis-Dusenbery BN, Mordes DA, Burberry A, Steinbaugh MJ, Gamage KK, Kirchner R *et al* (2019) ALS-implicated protein TDP-43 sustains levels of STMN2, a mediator of motor neuron growth and repair. *Nat Neurosci* 22: 167–179

Krach F, Batra R, Wheeler EC, Vu AQ, Wang R, Hutt K, Rabin SJ, Baughn MW, Libby RT, Diaz-Garcia S *et al* (2018) Transcriptome–pathology correlation identifies interplay between TDP-43 and the expression of its kinase CK1E in sporadic ALS. *Acta Neuropathol* 136: 405–423

Kremer JR, Mastronarde DN, McIntosh JR (1996) Computer visualization of three-dimensional image data using IMOD. *J Struct Biol* 116: 71–76

Laferrière F, Maniecka Z, Pérez-Berlanga M, Hruska-Plochan M, Gilhespy L, Hock E-M, Wagner U, Afroz T, Boersema PJ, Barmettler G *et al* (2019) TDP-43 extracted from frontotemporal lobar degeneration subject brains displays distinct aggregate assemblies and neurotoxic effects reflecting disease progression rates. *Nat Neurosci* 22: 65–77

Lashley T, Rohrer JD, Mead S, Revesz T (2015) Review: An update on clinical, genetic and pathological aspects of frontotemporal lobar degenerations. *Neuropathol Appl Neurobiol* 41: 858–881

Lee EB, Porta S, Michael Baer G, Xu Y, Suh EunRan, Kwong LK, Elman L, Grossman M, Lee V-Y, Irwin DJ *et al* (2017) Expansion of the classification of FTLD-TDP: distinct pathology associated with rapidly progressive frontotemporal degeneration. *Acta Neuropathol* 134: 65–78

Lewis AJ, Genoud C, Pont M, van de Berg WD, Frank S, Stahlberg H, Shahmoradian SH, Al-Amoudi A (2019) Imaging of post-mortem human brain tissue using electron and X-ray microscopy. *Curr Opin Struct Biol* 58: 138–148

Li H-Y, Yeh P-A, Chiu H-C, Tang C-Y, Tu BP (2011) Hyperphosphorylation as a defense mechanism to reduce TDP-43 aggregation. *PLoS One* 6: e23075

Li Q, Babinchak WM, Surewicz WK (2021) Cryo-EM structure of amyloid fibrils formed by the entire low complexity domain of TDP-43. *Nat Commun* 12: 1620

Ling JP, Pletnikova O, Troncoso JC, Wong PC (2015) TDP-43 repression of nonconserved cryptic exons is compromised in ALS-FTD. *Science* 349: 650–655

Ling SC, Polymenidou M, Cleveland DW (2013) Converging mechanisms in ALS and FTD: disrupted RNA and protein homeostasis. *Neuron* 79: 416–438

Lövestam S, Schweighauser M, Matsubara T, Murayama S, Tomita T, Ando T, Hasegawa K, Yoshida M, Tarutani A, Hasegawa M *et al* (2021) Seeded assembly in vitro does not replicate the structures of α-synuclein filaments from multiple system atrophy. *FEBS Open Bio* 11: 999–1013

Maharana S, Wang J, Papadopoulos DK, Richter D, Pozniakovsky A, Poser I, Bickle M, Rizk S, Guillén-Boixet J, Franzmann TM *et al* (2018) RNA buffers the phase separation behavior of prion-like RNA binding proteins. *Science* 360: 918–921

Mann JR, Gleixner AM, Mauna JC, Gomes E, DeChellis-Marks MR, Needham PG, Copley KE, Hurtle B, Portz B, Pyles NJ *et al* (2019) RNA binding antagonizes neurotoxic phase transitions of TDP-43. *Neuron* 102: 321–338

Mastronarde DN (2005) Automated electron microscope tomography using robust prediction of specimen movements. *J Struct Biol* 152: 36–51

Meier BH, Riek R, Böckmann A (2017) Emerging structural understanding of amyloid fibrils by solid-state NMR. *Trends Biochem Sci* 42: 777–787

Melamed Ze'ev, López-Erauskin J, Baughn MW, Zhang O, Drenner K, Sun Y, Freyermuth F, McMahon MA, Beccari MS, Artates JW *et al* (2019) Premature polyadenylation-mediated loss of stathmin-2 is a hallmark of TDP-43-dependent neurodegeneration. *Nat Neurosci* 22: 180–190

Meng F, Yoo J, Chung HS (2020) Heterogeneous aggregation of amyloid-β 42 from single-molecule spectroscopy. *bioRxiv* https://doi.org/10.1101/2020.09.10.290023 [PREPRINT]

Murray DT, Kato M, Lin Y, Thurber KR, Hung I, McKnight SL, Tycko R (2017) Structure of FUS protein fibrils and its relevance to self-assembly and phase separation of low-complexity domains. *Cell* 171: 615–627

Neumann M, Kwong LK, Lee EB, Kremmer E, Flatley A, Xu Y, Forman MS, Troost D, Kretzschmar HA, Trojanowski JQ *et al* (2009) Phosphorylation of S409/410 of TDP-43 is a consistent feature in all sporadic and familial forms of TDP-43 proteinopathies. *Acta Neuropathol* 117: 137–149

Neumann M, Sampathu DM, Kwong LK, Truax AC, Micsenyi MC, Chou TT, Bruce J, Schuck T, Grossman M, Clark CM *et al* (2006) Ubiquitinated TDP-43 in frontotemporal lobar degeneration and amyotrophic lateral sclerosis. *Science* 314: 130–133

Nonaka T, Masuda-Suzukake M, Arai T, Hasegawa Y, Akatsu H, Obi T, Yoshida M, Murayama S, Mann D, Akiyama H *et al* (2013) Prion-like properties of pathological TDP-43 aggregates from diseased brains. *Cell Rep* 4: 124–134

Nonaka T, Suzuki G, Tanaka Y, Kametani F, Hirai S, Okado H, Miyashita T, Saitoe M, Akiyama H, Masai H *et al* (2016) Phosphorylation of TAR DNA-binding protein of 43 kDa (TDP-43) by truncated casein kinase 1δ triggers mislocalization and accumulation of TDP-43. *J Biol Chem* 291: 5473–5483

Pérez-Berlanga M, Laferrière F, Polymenidou M (2019) SarkoSpin: a technique for biochemical isolation and characterization of pathological TDP-43 aggregates. *Bio-Protocol* 9: e3424

Pettersen EF, Goddard TD, Huang CC, Couch GS, Greenblatt DM, Meng EC, Ferrin TE (2004) UCSF Chimera – a visualization system for exploratory research and analysis. *J Comput Chem* 25: 1605–1612

Polymenidou M, Cleveland DW (2011) The seeds of neurodegeneration: prion-like spreading in ALS. *Cell* 147: 498−508

Polymenidou M, Lagier-Tourenne C, Hutt KR, Huelga SC, Moran J, Liang TY, Ling S-C, Sun E, Wancewicz E, Mazur C *et al* (2011) Long pre-mRNA depletion and RNA missplicing contribute to neuronal vulnerability from loss of TDP-43. *Nat Neurosci* 14: 459−468

Porta S, Xu Y, Restrepo CR, Kwong LK, Zhang B, Brown HJ, Lee EB, Trojanowski JQ, Lee VM-Y (2018) Patient-derived frontotemporal lobar degeneration brain extracts induce formation and spreading of TDP-43 pathology in vivo. *Nat Commun* 9: 4220

Porta S, Xu Y, Lehr T, Zhang B, Meymand E, Olufemi M, Stieber A, Lee EB, Trojanowski JQ, Lee VM-Y (2021) Distinct brain-derived TDP-43 strains from FTLD-TDP subtypes induce diverse morphological TDP-43 aggregates and spreading patterns in vitro and in vivo. *Neuropathol Appl Neurobiol* https://doi.org/10.1111/nan.12732

Schindelin J, Arganda-Carreras I, Frise E, Kaynig V, Longair M, Pietzsch T, Preibisch S, Rueden C, Saalfeld S, Schmid B *et al* (2012) Fiji: an open-source platform for biological-image analysis. *Nat Methods* 9: 676−682

Scialò C, Tran TH, Salzano G, Novi G, Caponnetto C, Chiò A, Calvo A, Canosa A, Moda F, Caroppo P *et al* (2020) TDP-43 real-time quaking induced conversion reaction optimization and detection of seeding activity in CSF of amyotrophic lateral sclerosis and frontotemporal dementia patients. *Brain Commun* 2: fcaa142

Shahmoradian SH, Lewis AJ, Genoud C, Hench J, Moors TE, Navarro PP, Castaño-Díez D, Schweighauser G, Graff-Meyer A, Goldie KN *et al* (2019) Lewy pathology in Parkinson's disease consists of crowded organelles and lipid membranes. *Nat Neurosci* 22: 1099−1109

Shenoy J, El Mammeri N, Dutour A, Berbon M, Saad A, Lends A, Morvan E, Grélard A, Lecomte S, Kauffmann B *et al* (2020) Structural dissection of amyloid aggregates of TDP-43 and its C-terminal fragments TDP-35 and TDP-16. *FEBS J* 287: 2449−2467

Shi Y, Zhang W, Yang Y, Murzin A, Falcon B, Kotecha A, Van Beers M, Tarutani A, Kametani F, Garringer HJ *et al* (2021) Structure-based classification of tauopathies. *Nature* 598: 359−363

Shimonaka S, Nonaka T, Suzuki G, Hisanaga SI, Hasegawa M (2016) Templated aggregation of TAR DNA-binding protein of 43 kDa (TDP-43) by seeding with TDP-43 peptide fibrils. *J Biol Chem* 291: 8896−8907

Silva LAG, Simonetti F, Hutten S, Riemenschneider H, Sternburg EL, Pietrek LM, Gebel J, Doetsch V, Edbauer D, Hummer G *et al* (2021) Disease-linked TDP-43 hyperphosphorylation suppresses TDP-43 condensation and aggregation. *bioRxiv* https://doi.org/10.1101/2021.04.30.442163 [PREPRINT]

Tan RH, Shepherd CE, Kril JJ, McCann H, McGeachie A, McGinley C, Affleck A, Halliday GM (2013) Classification of FTLD-TDP cases into pathological subtypes using antibodies against phosphorylated and non-phosphorylated TDP43. *Acta Neuropathol Commun* 1: 33

Tollervey JR, Curk T, Rogelj B, Briese M, Cereda M, Kayikci M, König J, Hortobágyi T, Nishimura AL, Župunski V *et al* (2011) Characterizing the RNA targets and position-dependent splicing regulation by TDP-43. *Nat Neurosci* 14: 452−458

Vasili E, Dominguez-Meijide A, Outeiro TF (2019) Spreading of α-synuclein and tau: a systematic comparison of the mechanisms involved. *Front Mol Neurosci* 12: 107

Vielhaber E, Virshup DM (2001) Casein kinase I: from obscurity to center stage. *IUBMB Life* 51: 73−78

Wang A, Conicella AE, Schmidt HB, Martin EW, Rhoads SN, Reeb AN, Nourse A, Ramirez Montero D, Ryan VH, Rohatgi R *et al* (2018) A single N-terminal phosphomimic disrupts TDP-43 polymerization, phase separation, and RNA splicing. *EMBO J* 37: e97452

Warnecke A, Sandalova T, Achour A, Harris RA (2014) PyTMs: a useful PyMOL plugin for modeling common post-translational modifications. *BMC Bioinformatics* 15 https://doi.org/10.1186/s12859-014-0370-6

Watanabe-Nakayama T, Nawa M, Konno H, Kodera N, Ando T, Teplow DB, Ono K (2020) Self- and cross-seeding on α-synuclein fibril growth kinetics and structure observed by high-speed atomic force microscopy. *ACS Nano* 14: 9979−9989

Xiao S, Sanelli T, Dib S, Sheps D, Findlater J, Bilbao J, Keith J, Zinman L, Rogaeva E, Robertson J (2011) RNA targets of TDP-43 identified by UV-CLIP are deregulated in ALS. *Mol Cell Neurosci* 47: 167−180

Zbinden A, Pérez-Berlanga M, De Rossi P, Polymenidou M (2020) Phase separation and neurodegenerative diseases: a disturbance in the force. *Dev Cell* 55: 45−68